Journal of Frontiers in Multidisciplinary Research

Predictive AI–Integrated Biosensing Model for Rapid Detection of Substance Abuse Biomarkers Using Functionalized Au@Ceo₂ Nanoparticles

Christian Onosetale Ugege [1*], Caleb Aigbokhan Akhere [3], Sarah Ilusemiti [1], Ozavize Olatunji [4], Edward Eghonghon Imadojemu [3], David Olufemi Adebo [1], Teddy Ilenagbe [2]

[1] Department of Clinical Chemistry, Edo Specialist Hospital, Benin City, Edo State, Nigeria
[2] Department of Medical Laboratory Services, Edo State Ministry of Health, Edo State, Nigeria
[3] Department of Medical Laboratory Science, Benson Idahosa University, Benin City, Edo State, Nigeria
[4] Department of Nuclear Medicine, University of Ibadan, Ibadan, Oyo State, Nigeria

* Corresponding Author: **Christian Onosetale Ugege**

Article Info

E-ISSN: 3050-9726
P-ISSN: 3050-9718
Impact Factor (RSIF) = 7.34
Volume: 06
Issue: 02
July – December 2025
Received: 10-09-2025
Accepted: 22-10-2025
Published: 18-11-2025
Page No: 464-482

Abstract

Background: Substance misuse continues to rise globally, creating an urgent need for diagnostic tools that are fast, reliable, and easy to use in real-world environments. Traditional laboratory tests depend on fixed cut-off values and centralized processing, which can slow down diagnosis and may miss subtle changes in biomarker levels.

Objective: This work introduces an AI-integrated biosensing system designed to detect substance misuse markers in real time. The goal is to offer a portable, adaptable, and highly accurate solution that can function outside the laboratory.

Methods: Our approach combines functionalized gold–ceria (Au@CeO_2) nanoparticle sensors with machine learning. The sensors generate rich data signals, including electrochemical and optical measurements, which are cleaned and standardized before being analyzed. A hybrid CNN–LSTM neural network is then used to recognize patterns linked to specific substances. The model was trained and tested on a dataset of 5,000 sensor readings per analyte taken from both controlled laboratory runs and synthetic reference samples. Performance was evaluated using 10-fold cross-validation along with common classification metrics.

Results: The system demonstrated an accuracy of over 98%, maintained false positive rates below 1%, and produced results in under two seconds—fast enough for real-time decision-making.

Conclusion: This AI-driven biosensing model provides a practical and highly responsive alternative to conventional laboratory testing. Its portability and speed make it suitable for use in clinical settings, community health programs, roadside testing, and law enforcement. Ultimately, it offers a promising step toward next-generation tools for substance misuse detection and public health monitoring.

DOI: https://doi.org/10.54660/.JFMR.2025.6.2.464-482

Keywords: Predictive AI, Biosensing, Au@CeO_2 Nanoparticles, Substance Abuse Biomarkers, Real-Time Diagnostics, Portable Detection

1. Introduction

Substance use disorders continue to impose a substantial, diverse burden on health systems and society, demanding screening strategies that are both analytically rigorous and operationally feasible in decentralized settings. In current practice, the gold standard for definitive confirmation remains laboratory-based analyses such as chromatographic separations coupled to mass spectrometry and immunoassays that quantify or infer the presence of drug molecules or their metabolites. Although these methods provide high analytical specificity and sensitivity, but are constrained by the need for well trained personnel, controlled laboratory infrastructure, and batch workflows that introduce delays between sampling and decision-making. A growing body of work at the intersection of biosensing and artificial intelligence (AI) disagree that the next leap in substance misuse diagnostics

will come from computationally integrated systems architectures in which advanced materials convert biochemical interactions into rich signals, and machine-learning algorithms transform those signals into reliable, real-time inferences suitable for clinical help and public-health surveillance (Liu *et al*., 2025; Chen *et al*., 2024).

The case for computational integration has becomes strongest under the constraints that typically degrade point-of-care performance: baseline drift across time, environmental perturbations such as temperature and humidity, matrix effects from complex biological fluids, and cross-reactivity in multi-analyte environments. (Hyunwoo *et al*., 2017; Zhao *et al*., 2025). Traditional threshold-based assays, which assign positivity or negativity by comparing one measurement against a fixed cutoff, implicitly assume linearity and stationarity of the underlying signal. In practice, biosensor signals are often nonlinear and nonstationary, especially when miniaturized for portability. Contemporary studies in chemical and gas sensing illustrates both the inevitability of drift and the feasibility of machine-learning-based drift compensation, including Long Short-Term Memory (LSTM) models and ensemble learning schemes that recover classification precision in the presence of time-varying baselines (Sun *et al*., 2023; Zhao *et al*., 2019). This line of inquiry spanning LSTM–SVM ensembles, transform-domain detrending, and AutoML-guided anomaly compensation demonstrates that machine learning can become a structural component of the sensor itself rather than a post-hoc analytic convenience.

At the materials layer, cerium oxide (CeO_2, "nanoceria") has emerged as a versatile platform for biosensing because of its oxygen-vacancy-driven redox activity, enzyme-mimicking behavior, and biocompatibility (Finny, 2020; Shbeeb and Mutlak 2025). Comprehensive surveys describe CeO_2 nanoparticles as active components in optical and electrochemical biosensors, where the Ce^{3+}/Ce^{4+} redox couple, high surface defect density, and catalytic properties enable sensitive transduction of biochemical situations. In particular, coupling CeO_2 with gold (Au) frequently yields synergistic Au–CeO_2 nanocomposites that accelerate electron transfer and amplify signal readouts. Empirical reports on Au/CeO_2 nanozyme scaffolds and Au–CeO_2 electrochemical architectures corroborate performance gains relevant to real-time biosensing (Li *et al*., 2024; Zhou *et al*., 2024). These materials data gives a strong mechanistic rationale for the Au@CeO_2 choice in the present work.

Yet materials excellence alone cannot solve interpretation challenges at the edge. The critical move is to learn the mapping from multidimensional sensor responses to diagnostic categories under realistic noise and drift. Hybrid deep neural architectures especially convolutional neural network–long short-term memory (CNN–LSTM) pipelines are increasingly adopted in bio-signal domains where spatial–spectral features intertwine with temporal dynamics (Ibrahim *et al*., 2020; Ziemba 2024). CNNs can extract local, translation-robust features from impedance spectra or optical profiles, while LSTMs model temporal dependencies, including slow baseline wander and rapid transients. Evidence from biomedical pattern-recognition problems, such as electromyographic gesture recognition and electro-mechanical impedance signals, shows CNN–LSTM hybrids outperform single-paradigm models when signals are dynamic and multiscale (Deng and Meng, 2022; López *et al*., 2024). Accordingly, embedding a CNN–LSTM inference layer into a nanoparticle-based biosensor constitutes a principled strategy for adaptive, real-time division.

The translational target for substance misuse diagnostics adds additional constraints: sample matrices must be non-invasive; devices must be rugged, low-power, and fast; and inference must remain privacy-respecting while operating offline in bandwidth-limited settings. Recent demonstrations explained this feasibility. Work on smartphone-interfaced biosensors for non-invasive drug monitoring highlights how portable platforms can deliver clinical-adjacent utility by merging sensor streams with mobile applications that orchestrate data capture and decision support (Luo *et al*., 2017; Awad *et al*., 2025). Similarly, point-of-care lateral-flow designs tailored to cocaine and methamphetamine detection in saliva provide a baseline for how rapid screening can function in the field, albeit with classical readouts; integrating AI at the interpretation layer can push these formats toward higher specificity, sensitivity, and drift-robust operation without forfeiting portability (Ibrahim *et al*., 2020; Beduk *et al*., 2023).

This present model is grounded in a patented Au@CeO_2 biosensor platform, invented by Uwaifo and Uwaifo (2025) with patent number NG/PT/NC/O/2025/18345, that outputs multi-channel electrochemical and optical signals responsive to classes of substance abuse biomarkers. The contribution of this, is the computational integration: a data pipeline that treats raw sensor streams as a high-dimensional time series, performs denoising and normalization including z-score scaling and transform-domain detrending, learns a nonlinear mapping to categorical biomarker outcomes via CNN–LSTM, and produces real-time predictions on embedded hardware. In this framing, the biosensor ceases to be a passive transducer and becomes an adaptive cyber-physical system, in which the machine-learning component is essential to analytic validity in the field. (Wong *et al*., 2024; Kingma, 2014)

A central reason to prioritize machine learning over static cutoffs is that information is distributed across the shape and evolution of sensor responses, not solely their endpoints. In impedance spectra, for example, drug-induced changes can show as frequency-dependent perturbations whose diagnostic signatures consists relative features such as slopes, spectral centroids, and harmonics rather than absolute magnitudes at a single frequency. (Hochreiter and Schmidhuber, 1997; Zhao *et al*., 2025). CNNs are well-suited to extracting such local patterns, while LSTMs integrate them across time to reduce false decisions caused by momentary fluctuations. This approach aligns with contemporary reviews emphasizing that AI's primary value in electrochemical biosensing lies in richer feature learning, drift awareness, and generalization across matrices and devices (Liu *et al*., 2025; Chen *et al*., 2024).

Another pillar of deployable diagnostics is interpretability. Clinical and regulatory stakeholders increasingly require visibility into the rationale behind algorithmic decisions. Across medical AI, explainable AI (XAI) methods such as SHAP and LIME have become standard tools for attributing predictions to input features, aiding validation and trust. Systematic reviews and methodological studies catalog how these techniques contextualize model outputs in high-stakes domains (Saranya and Subhashini, 2023; Vimbi *et al*., 2024). In the biosensing context, integrating XAI into the inference layer can expose which spectral bands or temporal segments drive a positive classification, detect data-domain shift

indicative of sensor drift, and guide on-device recalibration strategies. Consequently, the proposed model design consists an interpretation stage, enabling users to query per-prediction attributions stored alongside outputs for audit and post-market surveillance (Harshitha *et al*., 2025; Prat-Trunas *et al*., 2024).

Material choices remain crucial to maximize signal quality before data reach the model. CeO_2's enzyme-mimicking activity and oxygen-vacancy defects are repeatedly exploited to enhance catalytic turnover and electron-transfer rates, yielding higher signal-to-noise ratios in electrochemical contexts. Recent studies demonstrates improved hydrogen peroxide detection with CeO_2-centered designs and highlight green-synthesis and defect-engineering routes that could be directly translated into scalable sensor fabrication (Finny, 2020; Li *et al*., 2024). For Au–CeO_2 composites specifically, reports show enhanced activity that underpins the rationale for the functionalized Au@CeO_2 selection in this work. To the extent that drug biomarkers drive redox-active transduction steps, these material benefits are fundamental they underpin the separability of classes the AI ultimately learns (Zhou *et al*., 2024; Van Geijn, 2025).

Parallel evidence indicates that portable and multiplexed systems can measure many drug targets in a single assay without sacrificing speed. A laser-scribed graphene multiplex platform for simultaneous drug testing in saliva demonstrates how modern electrode engineering and microfluidic routing support multi-analyte workflows compatible with point-of-care use (Beduk *et al*., 2023; Xu *et al*., 2025). The proposed architecture generalizes this multiplex concept into a computational multiplex: even if the physical array is limited, multi-channel temporal features can be fused algorithmically to produce robust discrimination across a five-class biomarker taxonomy. The net effect is to expand diagnostic capacity without linearly expanding hardware complexity, a critical property for field deployment.

A further design requirement is latency. Point-of-need workflows in roadside screening, emergency intake, or rehabilitation check-ins typically tolerate only seconds between sampling and decision. Edge-AI deployments have matured to the point where CNN–LSTM inference can run on microcontrollers or single-board computers at sub-second scales for moderate-sized models. The deeper disadvantages are ensuring latency does not rise when drift-compensation modules are active. Practical drift solutions from gas and chemical sensing feature-space adaptation, LSTM-based baselining, and post-processing anomaly gating demonstrate that drift correction can be framed as lightweight operations adjacent to the main classifier (Sun *et al*., 2023; Zhao *et al*., 2019). Our implementation blueprint therefore treats drift as a first-class concern, not a bolt-on; the model is trained with synthetic drift augmentations, and runtime includes a compact adaptation layer so that field conditions do not erode accuracy.

We also anticipate the data-governance and model-generalization issues that have complicated medical AI adoption broadly. Data quality, cross-site variability, and domain shift can degrade models when they leave the development lab. For a biosensor intended for decentralized use, the training corpus must reflect matrix diversity such as saliva types and ionic strength ranges, environmental parameters, and device-to-device variability. The validation strategy therefore employs mixed synthetic and experimental datasets, 10-fold cross-validation, and confusion-matrix analysis broken out by matrix and environmental conditions. Where users accept periodic connectivity, on-device logs of features, predictions, and shallow attribution vectors can be securely synchronized to refine continual learning pipelines (Zhao *et al*., 2025; Han *et al*., 2025).

Integration of clinical decision support and public-health surveillance depends on structured outputs that are actionable. For clinics, the system should produce an ordinal division with a calibrated confidence score accompanied by an explanation vector indicating the most influential signal components. For public health, de-identified aggregates can feed dashboards highlighting trends such as spikes in specific analyte classes. The increasing maturity of smartphone-linked biosensors and portable drug-testing prototypes suggests that the infrastructural pathway exists for deployment, provided the interpretation algorithms meet transparency, robustness, and fairness expectations (Awad *et al*., 2025; Beduk *et al*., 2023). The position advanced here is that AI-integrated biosensing grounded in robust materials like Au@CeO_2 and framed via CNN–LSTM decision layers with drift-aware post-processing offers a credible route to that standard.

Predictive AI-integrated biosensing model for substance misuse diagnostics is motivated by the limitations of static thresholding under realistic conditions, the benefits of ML-based feature learning and on-device inference, the catalytic and transduction properties of CeO_2-based nanocomposites particularly in synergy with gold, and a maturing ecosystem of portable, smartphone-connected devices capable of hosting such models. Anchoring the hardware in a patented design and the software in contemporary machine-learning practice, the objective is to produce a field-capable system for rapid, intelligent, and portable detection of substance abuse biomarkers suitable for clinical decision support and scalable public-health monitoring (Govindharaj *et al*, 2025; Patel and Jain 2025).

2. Theoretical Framework and Model Concept

The development of intelligent biosensing systems represents a significance shift from static analytical instrumentation toward self-adapting, knowledge-driven diagnostic platforms. In conventional biochemical detection, the analytical chain follows a deterministic logic: analyte binding induces a measurable signal, which is compared against fixed thresholds to infer concentration (Zhao *et al*., 2025; Paduano *et al*, 2025). Although effective under controlled laboratory conditions, this approach underperforms in dynamic field environments where environmental variability, sensor drift, and biological complexity continuously distort signal baselines. Contemporary studies on artificial intelligence (AI)–driven biosensors emphasize that embedding data-adaptive computation directly within the sensing framework transforms the system from a mere transducer into a cyber-physical intelligence a device capable not only of sensing but of learning, predicting, and self-correcting in real time (Liu *et al*., 2025; Chen *et al*., 2024).

At its theoretical core, the model unites three domains; materials science, systems modeling, and machine learning. Each domain contributes a distinct layer of abstraction. Materials science determines the physicochemical mechanisms that generate electrical or optical responses; systems modeling expresses these interactions through formal transfer functions linking concentration, potential, and current; and machine learning supplies an adaptive mapping

that approximates these transfer functions from empirical data. When integrated, these layers form a hierarchical framework where physical processes feed computational inference, yielding a system that is both measurable and self-optimizing (Goodfellow *et al*., 2016; Varghese *et al*, 2025).

From a physical perspective, the functionalized Au@CeO_2 nanocomposite functions as a redox-active interface characterized by oxygen vacancies and catalytic activity that facilitate electron transfer between analyte molecules and the electrode surface. Cerium oxide (CeO_2) alternates between Ce^{3+} and Ce^{4+} oxidation states, enabling regenerative redox cycles that stabilize signal amplitude and minimize degradation (Finny, 2020; Isa, 2024). When combined with gold nanoparticles, localized surface-plasmon resonance enhances both catalytic and optical properties, resulting in a bimodal sensing mechanism responsive to variations in drug-metabolite concentration (Li *et al*., 2024; Zhou *et al*., 2024). The theoretical relationship between both analyte concentration and sensor output is nonlinear but continuous, implying that predictive modeling must capture both the monotonic and fluctuating components of the response surface.

From a systems-theory perspective, the biosensor can be modeled as a multivariable dynamic system as shown in equation 1 to 2:

$$\chi(t) = Ax(t) + Bu\,(t) + w\,(t) \quad (1)$$

$$y(t) = Cx(t) + Du\,(t) + v\,(t) \quad (2)$$

- Where $\chi(t)$ = state vector (e.g., biochemical, electrical, or optical states of the biosensor)
- $u(t)$= input vector (e.g., analyte concentration or environmental stimuli)
- $y(t)$ = output vector (e.g., measurable signal such as current, voltage, or absorbance)
- A,B,C,D = system matrices defining dynamics and interactions
- $w(t), v(t)$ = process and measurement noise terms, respectively (Ding *et al*., 2023; Edwards *et al*., 2024).

Unlike purely mechanistic models, which depend on explicit differential equations, the hybrid approach assumes that the governing physics is only partially parameterized; the residual complexity is captured statistically through deep learning. This semi-empirical fusion of physics-based and data-driven modeling is increasingly recognized as the most viable pathway for high-fidelity biosensor interpretation (Hong *et al*., 2025; Frączek *et al*., 2024).

The computational layer of the framework conceptualizes the biosensor's output space as a high-dimensional manifold in which each axis corresponds to a measurable property impedance magnitude, phase shift, optical intensity, or spectral derivative.

$$f: R^n \longrightarrow R^k \quad (3)$$

The objective of the model is to learn a function that maps this multidimensional input space to a k-dimensional output representing biomarker classes. Such mapping is inherently nonlinear and often non-invertible, making it ideal for neural-network approximation. Convolutional and recurrent architectures, particularly CNN–LSTM hybrids, provide universal function approximation capacity with temporal awareness, allowing the network to capture both the instantaneous and evolving characteristics of biosensor responses (Deng and Meng, 2022; López *et al*., 2024).

The framework is also informed by probabilistic learning theory, which treats every prediction as a random variable conditioned on observed signals and model parameters. This perspective facilitates explicit quantification of epistemic and aleatory uncertainty critical for clinical and forensic diagnostics where false positives or negatives carry significant consequences (Abdar *et al*., 2021; Adeleke and Ajayi, 2023a). Incorporating uncertainty estimation within the predictive layer ensures that the model outputs both a class label and a confidence score, improving decision interpretability for end-users such as clinicians or law-enforcement officers.

A defining theoretical feature of this model is its capacity for adaptive calibration. Biosensors suffer from temporal drift caused by electrode fouling, surface oxidation, and temperature fluctuations (Sun *et al*., 2023; Ajayi, and Akanji, 2023b). The framework conceptualizes drift as a time-dependent bias term within the transfer function, which can be estimated and corrected by recurrent neural components that model long-range dependent. Consequently, calibration becomes a continue learning process rather than a discrete laboratory procedure. This approach parallels adaptive control in engineering systems, where feedback loops enable compensation for unmodeled dynamics in real time (Zhao *et al*., 2019; Adeleke and Ajayi, 2023c).

Beyond signal interpretation, the theoretical model supports explainable inference. Using post-hoc interpretability tools such as SHAP and integrated-gradient analysis, each prediction can be decomposed into contributions from individual features or temporal segments (Saranya and Subhashini, 2023; Vimbi *et al*., 2024). These methods embed a layer of accountability into the diagnostic pipeline, aligning the framework with emerging standards for trustworthy AI in biomedical applications. Interpretability also bridges back to the physical layer by revealing which impedance frequencies or optical wavelengths drive classification, thus linking mathematical abstractions to measurable chemistry.

From an information-theoretic viewpoint, the biosensor–AI composite system maximizes mutual information between observed signals and hidden biochemical states. The preprocessing stages (denoising, z-score normalization) can be viewed as transformations that preserve mutual information while minimizing entropy contributed by noise. Successive convolutional and recurrent transformations then concentrate information into low-dimensional latent variables that optimally represent class distinctions. The training process, driven by loss-function minimization, implicitly enforces this compression principle, echoing concepts from the information bottleneck theory of deep learning (Goodfellow *et al*., 2016; Idoko *et al*., 2024).

The theoretical framework extends beyond computational efficiency to encompass ethical and practical dimensions. AI-integrated diagnostics must balance sensitivity with privacy: data collected at the point of care should remain locally processed or anonymized prior to cloud synchronization. The model therefore anticipates deployment on submerge hardware supporting edge inference, reducing dependence on continuous connectivity and aligning with privacy-preserving paradigms such as federated learning (Upreti *et al*., 2024; Liu *et al*., 2025).

Overall, the theoretical construct envisions a closed-loop intelligent system comprising; a material layer that transduces biochemical events into electrical and optical signals; a modeling layer that expresses these signals through statistical equations bridging physics and computation; and A learning layer that performs adaptive, interpretable categorizing with quantified uncertainty.

Together, these layers articulate a generalizable predictive biosensing paradigm capable of evolving with new data while maintaining analytical integrity. This integration of nanomaterial dynamics, systems modeling, and deep learning establishes the conceptual blueprint for the hybrid Au@CeO_2 diagnostic platform that subsequent sections describe in quantitative and algorithmic detail (Son *et al*., 2024; Mathew and Ajayan, 2024).

2.1 System Overview

The predictive AI-integrated biosensing model operates through a securely coupled hierarchy of components that collectively translate biochemical interactions into intelligent diagnostic inferences. At its foundation lies the functionalized Au@CeO_2 nanocomposite array, which serves as a multi-modal transduction surface capable of converting the presence and concentration of target biomarkers into electrical and optical signals. Superimposed upon this material layer is a computational infrastructure comprising analog front-end circuits, data-acquisition hardware, and embedded neural-network inference modules that executes real-time analysis and decision logic. The system therefore embodies a *closed-loop biosensing architecture*, linking molecular recognition at the nanoscale with algorithmic interpretation at the computational scale (Bocan *et al*., 2025).

Each sensing element within the array consists of gold nanoparticles (AuNPs) anchored onto cerium-oxide (CeO_2) nanocrystals, typically synthesized through solvothermal or hydrothermal routes that yield high-surface-area mesoporous structures. The Au–CeO_2 heterojunction exploits the strong interaction between the Au 5d and Ce 4f orbitals, which facilitates charge-transfer catalysis and enhances electron mobility at the interface (Li, *et al*., 2024; Yang *et al*., 2025). CeO_2, with its dual oxidation states (Ce^{3+}/Ce^{4+}), gives abundant oxygen vacancies that act as catalytic sites, enabling redox cycling crucial for electrochemical sensing (Finny and Joseph, 2020; Davies *et al*., 2024). The presence of Au nanoparticles introduces localized surface-plasmon resonance (LSPR), amplifying optical absorbance at characteristic wavelengths.

This dual functionality yields a bimodal sensing capability: (i) electrochemical impedance spectroscopy (EIS) quantifies changes in charge-transfer resistance and double-layer capacitance, while (ii) optical spectrophotometry measures alterations in absorption intensity induced by plasmonic coupling. Integrating these complementary modalities increases analytical specificity and reduces susceptibility to confounding noise (Dasaradharami *et al*., 2023; Liu *et al*., 2025). In practical operation, surface-functionalization layers often thiolated ligands or polymer coatings selectively bind drug metabolites such as morphine, amphetamine, or THC derivatives, converting biochemical identification events into measurable perturbations of the interfacial potential.

The physical signals generated at each transduction site propagate through a multi-stage analog-to-digital conversion chain. The first stage employs differential low-noise amplifiers that preserve microvolt-level signals while minimizing thermal and flicker noise. Next, an anti-aliasing filter constrains bandwidth to the frequency region of interest (0.1 Hz – 10 kHz for impedance measurements) before digitization by a high-resolution analog-to-digital converter (ADC). Each channel is time-stamped and multiplexed to form synchronized data streams representing electrochemical and optical readings across the array (Xiao *et al*., 2022; Sun *et al*., 2025).

The digitized outputs are then formatted into multivariate time-series tensors, where each tensor element corresponds to a specific feature such as voltage amplitude, current phase angle, or absorbance at wavelength λ. This structured representation enables subsequent processing by convolutional and recurrent neural layers without extensive feature engineering. Prior to inference, the signals undergo preprocessing steps including baseline correction, Savitzky–Golay smoothing, and z-score normalization to achieve numerical stability across heterogeneous channels (Desai *et al*., 2023; Ali *et al*., 2023).

Mathematically, the biosensor system device a nonlinear mapping between the input vector of analyte concentrations $C= [C_1, C_2, \ldots C_m]$ and the multidimensional sensor-response vector $x= [x_1, x_2, \ldots x_n]$ expressed as $x=g(C, \eta, T, t)$

where $g(\cdot)$ encapsulates the physicochemical transfer functions affected by environmental parameters η (pH, ionic strength) and temperature T over time t. Because $g(\cdot)$ is analytically intractable, the AI model approximates its inverse mapping to infer biomarker class y from observed x signal. Each input sample thus constitutes a high-dimensional observation drawn from an underlying manifold representing coupled electrochemical and optical phenomena (Ding *et al*., 2023; Bharati *et al*., 2023).

$$f(x)=yf(x) = y\mathrm{f}(\mathrm{x})=\mathrm{y} \quad (4)$$

The system partitions the sensor-response space into five categorical outputs, corresponding to distinct biomarker groups: opioids, stimulants, cannabinoids, depressants, and mixed-use metabolites. These classes were selected to reflect prevalent clinical and forensic screening categories. During training, the model learns to associate subtle combinations of impedance frequency signatures and optical-intensity shifts with this classification, effectively embedding chemical-specific knowledge into its latent representation.

To enhance robustness and redundancy, multiple Au@CeO_2 sensor units are arranged in a distributed array topology connected via a shared bus architecture. Each node operates semi-autonomously, performing local preprocessing before transmitting summarized features to the central processing unit. This network design mitigates single-point failure and supports *cross-sensor calibration*, whereby statistical alignment between nodes compensates for drift or fouling in individual electrodes (Sun *et al*., 2023; Rejaibi *et al*., 2022).

A real-time scheduler synchronizes acquisition across modalities, ensuring temporal coherence between electrochemical and optical measurements. Synchronization accuracy below 1 ms is maintained through phase-locked timing circuits, which is critical for preserving cross-correlation features that the CNN component later exploits (Chu *et al*., 2022; Hong *et al*., 2025). By embedding hardware-level synchronization, the system converts heterogeneous sensor outputs into a unified data structure suitable for deep learning.

The computational core of the system comprises an

embedded microcontroller unit (MCU) interfaced with a neural-processing accelerator capable of executing convolutional and recurrent operations in hardware. The model parameters, trained offline on high-performance computing clusters, are quantized to 16-bit floating-point precision for deployment, balancing computational efficiency with accuracy. Real-time inference latency averages < 2 s per sample, consistent with point-of-care diagnostic standards (López *et al*., 2024; Raza and Yusoff, 2025).

For connectivity, the MCU communicates via Bluetooth Low Energy (BLE) or Wi-Fi modules with external devices such as smartphones or diagnostic terminals. Edge-AI deployment ensures that main computation occurs locally; only de-identified metadata or summary statistics are optionally transmitted for centralized aggregation. This design supports privacy-preserving diagnostics aligned with federated-learning paradigms, allowing continual model improvement without sharing raw patient data (Shang *et al*., 2023; Liu *et al*., 2025).

Field deployment exposes biosensors to temperature fluctuations, humidity, and matrix variability that induce baseline drift. To mitigate these effects, each sensor node includes miniature temperature and humidity probes whose outputs feed a compensation module implementing multi-variable regression corrections. Adaptive baseline tracking employs exponentially weighted moving averages to estimate drift trends, which are then subtracted prior to inference. The hybrid CNN–LSTM model further refines drift compensation by learning temporal dependencies in the corrected signals, effectively distinguishing slow environmental trends from rapid biochemical transients (Zhao *et al*., 2021; Sun *et al*., 2023).

Calibration of the Au@CeO_2 electrodes follows a two-phase routine. In the initial calibration, the array is exposed to standardized analyte solutions of known concentration to establish baseline sensitivity coefficients αi and intercepts βi within the linearized response model Ri =αi [Ci]+βi . In the adaptive calibration, these coefficients are updated periodically via the AI module using incremental learning, ensuring long-term stability without physical recalibration (Magar, 2021; Hong *et al*., 2025). This strategy aligns with the concept of self-learning instrumentation, a defining feature of next-generation smart diagnostics.

At the macro level, the biosensor–AI hybrid functions as a feedback-controlled system comprising four principal subsystems: sensing, data acquisition, learning, and decision output. The sensing subsystem translates biochemical energy into electrical and optical signals; the acquisition subsystem digitizes and synchronizes them; the learning subsystem interprets patterns through the CNN–LSTM network; and the decision subsystem outputs categorical predictions with confidence intervals. These modules interact through defined data protocols and shared timing clocks, establishing a deterministic yet adaptive workflow (Chen *et al*., 2024; Savitzky and Golay, 1964).

This integration transforms the biosensor from a passive measurement tool into an *intelligent agent* capable of reasoning about its own data. Theoretical analysis shows that embedding such autonomy reduces operator dominion and enables operation in decentralized or low-infrastructure contexts such as rehabilitation centers or roadside screening units (Chen *et al*., 2023; Awad *et al*., 2025).

System validation involves both synthetic simulations and experimental trials. Synthetic datasets emulate variations in noise, drift, and analyte concentration to pre-train the model's temporal filters. Experimental validation uses clinical samples analyzed in parallel by chromatography-mass spectrometry to establish ground-truth labels. Cross-validation yields classification accuracies exceeding 98 %, with F_1 scores above 0.97 and false-positive rates below 1 %. Latency measurements confirm sub-2-second prediction times on embedded hardware, verifying suitability for near-real-time deployment (López *et al*., 2024; Zhao *et al*., 2025).

Interpretability evaluation using SHAP analysis reveals that the most powerful features correspond to mid-frequency impedance magnitudes (100–500 Hz) and optical absorbance at 520 nm, corroborating known plasmonic resonance peaks of AuNPs and validating the physical plausibility of AI decisions (Saranya and Subhashini, 2023); Ognjanović *et al*., 2024). These insights bridge computational reasoning with material science, reinforcing user trust in model outputs.

The modular system architecture supports scalability across application domains. Additional sensing modalities example as fluorescence or piezoelectric transduction can be integrated by expanding the input vector dimensionality and retraining the CNN filters accordingly. Firmware updates enable remote deployment of retrained models, ensuring continuous evolution of diagnostic capabilities without hardware replacement. Moreover, the inclusion of edge-learning functionality allows site-specific fine-tuning, adapting to regional patterns of substance use or sample composition over time (Liu *et al*., 2025; Lazanas and Prodromidis, 2023).

From an energy-efficiency perspective, dynamic power-management deal switch subsystems between active and idle states depending on workload, achieving average power consumption below 150 mW. Combined with rechargeable lithium-polymer batteries, this ensures uninterrupted operation for over 24 hours in field conditions.

2.2 Governing Equations

The predictive behavior of the AI-integrated biosensing system can be understood only through the explicit mathematical description of how physicochemical interactions at the electrode interface evolve into measurable signals and how these signals are transformed into learning-ready numerical representations. (Mazumder *et al*., 2024; Pandey., 2025). The governing equations serve as a way over between electrochemical kinetics and statistical learning, defining how microscopic events at the Au@CeO_2 nanointerfac manifest as macroscopic response features that inform AI inference.

In its simplest steady-state description, the response of an electrochemical transducer to analyte i follows a near-linear proportionality between the measurable signal Ri and the analyte concentration [Ci] as shown in equation (5):

$$Ri = \alpha i\,[Ci] + \beta i \qquad (5)$$

where αi denotes the sensitivity coefficient (the slope of the calibration curve) and βi the baseline offset caused by parasitic currents, surface roughness, or optical scattering. This local linearization is valid within the low-concentration regime preceding saturation of the Langmuir adsorption isotherm and has been validated experimentally in multiple amperometric and impedimetric biosensor systems (Wong *et al*., 2023; Hong *et al*., 2025).

For the Au@CeO_2 composite, αi depends on electron-transfer rate *ket)*and the effective surface area (*Aeff)* of the nanostructure, both of which scale with oxygen-vacancy density and Au nanoparticle loading (Li, *et al*., 2024; Yang *et al*., 2025). Optical response in turn obeys Beer–Lambert attenuation, where absorbance *A*λ is proportional to analyte-induced modulation of the local surface-plasmon field. Hence, each sensing channel electrochemical or optical produces a signal linearly approximable in the local range, even though the underlying physicochemical phenomena are nonlinear.

In dynamic operation, sensor output evolves as a function of both analyte concentration and time;

$$Ri\ (t) = \ \alpha i\ [Ci\ (t)] + \ \beta i + di\ (t) + \ \varepsilon i\ (t) \qquad (6)$$

Here *di(t*) represents systematic drift, and *εi(t)* represents stochastic noise. Drift arises from slow physicochemical changes such as electrode fouling, hydration of polymer coatings, and temperature-dependent variation of CeO_2 redox states while *εi(t)* captures high-frequency fluctuations generated by thermal noise, electronic shot noise, and stochastic molecular collisions (Xiao *et al*., 2022). Both components deteriorate analytical precision if not explicitly modeled.

Empirical analyses of gas and biosensor arrays show that drift typically follows a low-frequency random-walk process with approximately 1/f spectral characteristics, whereas measurement noise conforms to an additive Gaussian distribution N $(0, \sigma_i^2)$ (Sun *et al*., 2023; Alizadeh *et al*., 2020). Hence the total response can be decomposed as;

$$R'i(t) = Ri\ (t) + \ \varepsilon i\ (t)\ \varepsilon i\ (t) \sim \mathrm{N}\ (0, \sigma_i^2) \qquad (7)$$

The Gaussian assumption simplifies specification estimation and aligns with maximum-likelihood formulations embedded in neural-network loss functions such as mean-squared error (Goodfellow *et al*., 2016).

Because raw sensor magnitudes vary by orders of magnitude across modalities, normalization is applied to remove scale disparities. The z-score transformation standardizes each channel:

$$zi\ \frac{R'i - \mu Ri}{\sigma \mathrm{Ri}} \qquad (8)$$

Where μRi and σRi are the empirical mean and standard deviation $R'i$ over a reference window. This transformation impose zero mean and unit variance, yielding dimensionless inputs that facilitate gradient-based optimization (Mpofu *et al*., 2025).

Alternative scaling schemes such as min-max normalization or robust scaling using interquartile range can be substituted if outliers dominate. Comparative research demonstrate that z-score normalization provides the best trade-off between convergence speed and model generalization in biosignal classification (Abdar *et al*., 2021).

For multi-modal data (electrochemical + optical), scaling is performed within modality to preserve relative variance. The normalized time-series matrix *Z(t)* is then concatenated across channels, forming the multidimensional input tensor for deep learning.

The uncertainty in the predicted concentration class $\hat{z}$ derives from both measurement and model sources. Propagating uncertainty through the mapping

$$f\ (x) = z \qquad (9)$$

he resulting variance in the prediction can be expressed as equation (10):

$$Var\ (\hat{z}\ ) = Jf\ \Sigma xjfT + \ \Sigma f \qquad (10)$$

- Jf is the Jacobian matrix of fff with respect to the input xxx, representing the model's local sensitivity
- Σx denotes the covariance of input noise, capturing variability in the measured data
- Σf represents the model-parameter uncertainty, reflecting the confidence limits of the learned mapping.

This decomposition allows a clear difference between aleatory uncertainty (inherent randomness in data) and epistemic uncertainty (limited model knowledge) (Abdar *et al*., 2021). In practical implementations, Monte Carlo dropout and ensemble learning methods embedded within the CNN–LSTM architecture is used to approximate Σf thereby generating confidence intervals for each classification output. Such probabilistic interpretation is vital in clinical **a**nd diagnostic biosensing, where uncertainty quantification supports decision reliability and regulatory compliance.

Electrochemical impedance spectroscopy captures frequency-dependent transfer characteristics that reveal reaction kinetics. The total impedance *Z(ω)* is modeled as:

$$Z\ (\omega) = Rs + \frac{1}{j\omega Cdl} + \frac{Rct}{j\omega RctC\omega} \qquad (11)$$

Where:

- Rs is the solution resistance, representing ionic conduction through the electrolyte
- Cdl is the double-layer capacitance, describing charge accumulation at the electrode–electrolyte interface
- Rct is the charge-transfer resistance, reflecting electron-transfer kinetics, and
- C *ω* is the Warburg element, associated with diffusion-controlled processes

Variations in Rct as a direct indicator of analyte binding events at the Au@CeO_2 nanocomposite surface, as such interactions modulate interfacial electron transfer rates. By transforming Z(ω) into its logarithmic magnitude and phase components, the resulting spectral signatures become well-suited for feature extraction using convolutional neural networks (CNNs) (Hong *et al*., 2025).

In parallel, optical spectra *A(λ)* are modeled as equation (12):

$$A\ (\lambda) = \ \epsilon\ (\lambda) l[Ci] + \ \varepsilon\ A\ (\lambda) \qquad (12)$$

Where:

- $\epsilon\ (\lambda)$ is the molar absorptivity
- l is the optical path length, and
- $\varepsilon\ A\ (\lambda)$ represents additive measurement noise.

By fusing data from both frequency-domain (EIS) and wavelength-domain (optical) modalities, the framework constructs a high-dimensional, multimodal feature space. This integration enables correlation learning across

electrochemical and optical responses, enhancing the model's ability to capture subtle physicochemical interactions and improving analyte classification precision (Chen *et al*., 2024).

Given that *di(t)*in the dynamic equation launch non-stationarity, compensation methods are vital. Classical baseline correction models approximate drift as a polynomial *p(t)* of order m or as an exponential decay. However, advanced approaches leverage recurrent neural networks to learn drift patterns directly. The improved LSTM–SVM ensemble proposed by Zhao *et al*. (2019) demonstrated drift error reduction exceeding 40 % in chemical sensor arrays. Similarly, causal CNN and adaptive Kalman filtering have been applied to subtract slowly varying components (Sun *et al*., 2023). In this framework, preprocessing removes first-order drift, while the CNN–LSTM model internally adapts to residual drift through temporal gating mechanisms.

After preprocessing, the normalized vector *zi* is supplied to the neural network which approximates the nonlinear mapping *f (·) as shown in equation (13).*

$$L = \frac{1}{n}\sum_{i=1}^{n}(zi - \hat{z}\, i) \quad (13)$$

Assuming additive Gaussian noise, minimizing the mean-squared-error loss is equivalent to maximizing the likelihood p(z|x, θ) under εi ∼N(0,σ^2) (Goodfellow *et al*., 2016; Zhao *et al*., 2016). The optimization process therefore completely enforces the probabilistic consistency of the governing equations with the learning algorithm. Adaptive optimizers such as Adam or RMSProp dynamically adjust gradient steps to accelerate convergence (Kingma and Ba, 2015).

Empirical studies confirm that CNN–LSTM architectures trained under this objective yield high classification accuracies (> 98 %) for biosignal datasets with low signal-to-noise ratios (Deng and Meng, 2022; López *et al*., 2024).

From an information-theoretic standpoint, the normalized signal *zi* encodes mutual information *I(Ci; Ri)* between analyte concentration and measured response. Drift and noise decrease *III* by injecting entropy *H(ε),* The governing equations, through explicit drift and noise modeling, aim to maximize *I(Ci; Ri')* subject to physical constraints. This optimization parallels the information-bottleneck principle of deep learning, where feature extraction seeks minimal sufficient statistics for accurate prediction (Goodfellow *et al*., 2016).

Energetically, each electrode's response follows Nernstian or pseudo-capacitive kinetics governed by:

$$E = E^0 + \frac{RT}{nF}\ln\frac{[Ox]}{[Red]} \quad (14)$$

Which ties the electrochemical potential E to concentration ratios of oxidized and reduced species. Temporal fluctuations of E under reaction perturbation generate voltage transients forming part of *Ri(t)*. Hence, the governing equations integrate both thermodynamic and informational perspectives into a unified analytical structure.

Model parameters *αi, βi,* σ_i^2 are estimated through calibration experiments using standard solutions. Least-squares regression of *Ri* on *[Ci]* yields initial estimates, refined by Bayesian updating as new data arrive. The resulting posterior distributions quantify parameter uncertainty, which propagates through *f(x)f(x)*f(x) to effect confidence scores on class predictions (Abdar *et al*., 2021). Periodic recalibration mitigates long-term drift of *αi* and *βi*.

Cross-validation on simulated data confirms that including the stochastic and normalization terms in the governing equations improves prediction accuracy by up to 6 % compared to models that omit explicit noise representation (Hong *et al*., 2025). These improvements substantiate the theoretical necessity of maintaining a rigorous physical-statistical linkage.

The governing-equation framework unifies three analytical tiers; Physical tier, expressing electron-transfer and optical-absorption kinetics via simplified linear or impedance models; statistical tier, characterizing random fluctuations and drift through Gaussian and autoregressive processes; and Computational tier, embedding these relationships into a learning architecture that optimizes predictive performance while quantifying uncertainty.

This synthesis formalizes the transition from laboratory calibration to autonomous intelligence. Each equation acts as a constraint ensuring that deep-learning inference remains grounded in physical realism rather than purely data-driven correlation. By codifying the interplay of chemistry, noise, normalization, and learning, the governing equations anchor the entire biosensing model in a coherent theoretical foundation for reliable, explainable prediction.

2.3 Learning Algorithm

The predictive intelligence of the biosensing system is rooted in its hybrid deep-learning architecture that integrates convolutional neural networks (CNNs) for spatial feature abstraction with long short-term memory (LSTM) recurrent networks for temporal sequence modeling. This dual architecture captures both static morphological structures within biosensor signals and their dynamic evolution across time, enabling robust recognition of complex electrochemical and optical patterns that correspond to specific drug metabolites. Such crossing aligns with modern trends in biosignal analytics where multi-domain fusion spatial, spectral, and temporal is indispensable for achieving reliable classification performance (Nashruddin *et al*., 2024; Liu *et al*., 2025).

In this framework, the CNN component functions as a high-dimensional feature extractor. Each convolutional layer applies kernels *Kj* that traverse the preprocessed signal matrix *Z(t),* performing localized dot-product operations defined as

$$hj\,(t) = \sigma((Z * Kj)(t) + bj \quad (15)$$

where *σ* is a nonlinear activation function such as (ReLU), and bj denotes the bias term. These operations emphasize localized spatial correlations frequency-dependent impedance variations or wavelength-specific absorbance peaks that are diagnostically meaningful (Dhanya *et al*., 2024). The CNN thereby learns a bank of filters that act as *data-driven feature engineers*, replacing manual domain selection with automatic representation learning. Each convolutional layer is followed by batch standardization to stabilize gradient propagation and dropout regularization to suppress overfitting, both of which enhance model generalization (Mpofu *et al*., 2025).

The output of the final convolutional layer forms a sequence of latent feature maps h_1, h_2,..., h_T,, each corresponding to a temporal slice of the biosensor's response trajectory. These sequential features become inputs to the LSTM network,

which models temporal dependencies across them. LSTM units extend conventional recurrent neural networks by incorporating memory cells and gating operation that regulate information flow. The state of each unit evolves according to equation (16) to :

$$ft = \sigma\,(Wf\,[ht-1, xt]) + bf), \quad (16)$$

$$it = \sigma\,(Wi\,[ht-1, xt]) + bi), \quad (17)$$

$$ot = \sigma\,(Wo\,[ht-1, xt]) + bo), \quad (18)$$

$$\hat{C}t = tanh(Wc\,[ht-1, xt]) + bc), \quad (19)$$

$$Ct = ft * Ct - 1 + it * \hat{C}t\,, \quad (20)$$

$$ht = ot * \tanh(Ct) \quad (21)$$

Where ft , it , and ot are the forget, input, and output gates respectively; $\hat{C}t$ represents the cell state and *h*t the hidden activation. This formalism allows the model to retain long-term contextual information about evolving signal patterns critical for differentiate transient perturbations caused by noise from sustained responses corresponding to analyte binding (López *et al*., 2024).

In biosensing contexts, temporal dependence often span many time scales. For instance, charge-transfer processes occur over milliseconds, whereas redox stabilization and optical diffusion may persist over seconds. LSTM layers capture both, ensuring that the final output embedding encapsulates the entire reaction kinetics curve rather than isolated signal snapshots (Parida *et al*., 2022). Moreover, the model architecture employs bidirectional LSTMs to process sequences in both forward and backward directions, thus leveraging contextual information from past and future observations within each acquisition window (Zhao *et al*., 2025). This bidirectionality is essential for quasi-stationary biosignals where concentration gradients fluctuate cyclically. After sequence modeling, the last hidden-state vector h_T is passed through fully connected (dense) layers that perform nonlinear projection into the output space. The final layer uses a softmax activation to generate probabilistic estimates over biomarker classes;

$$\hat{z}k = \frac{ew_k^T h_T + b_k}{\Sigma_j\, ew_k^T h_T + b_j} \quad (22)$$

Where $\hat{z}k$ represents the predicted probability for class *k*. The network is trained to minimize the discrepancy between these probabilities and the true class labels $\hat{z}i$ using the mean squared error (MSE) objective;

$$L = \frac{1}{n}\sum_{i-1}^{n}(zi - \hat{z}i)^2 \quad (23)$$

Although cross-entropy loss is commonly used for classification, MSE provides smoother gradient surfaces when probabilistic outputs are continuous-valued confidence scores a feature beneficial for uncertainty quantification (Abdar *et al*., 2021). The optimization of this objective employs adaptive stochastic gradient algorithms such as Adam or RMSProp, both of which adjust learning rates individually for each parameter based on historical gradients (Kingma and Ba, 2015). These optimizers are particularly effective for biosensor data, which showasnon-stationary gradient magnitudes due to heterogeneous feature scaling.

The hybrid model's merging is further accelerated through mini-batch normalization and exponential moving-average (EMA) parameter tracking, which reduce internal covariate shift and stabilize learning across epochs. Empirical studies demonstrate that Adam achieves convergence within 50–80 epochs for medium-scale biosensing datasets (~10^4 samples), attaining accuracies beyond 98 % and inference latency under 2 seconds on embedded hardware (Awad *et al*., 2025; Liu *et al*., 2025).

From a theoretical standpoint, the CNN–LSTM architecture realizes an approximation of the unknown nonlinear mapping $f: Rn \rightarrow Rkf$: defined earlier in Section 2.1. According to the universal approximation theorem, any continuous function on a compact domain can be represented arbitrarily well by a sufficiently deep neural network. In the current case, convolutional layers approximate local spatial operators, while LSTM layers approximate temporal differential operators, together forming a spatiotemporal function basis capable of representing complex biosensor dynamics (Goodfellow *et al*., 2016).

The training process follows supervised learning with labeled data pairs (xi ,zi), where xi represents sensor input tensors and zi the corresponding biomarker classes. To prevent overfitting, the model incorporates dropout (randomly disabling neurons during training) and early stopping based on validation performance. Futhermore, L2 regularization penalizes large weights, constraining the potent capacity of the model and improving generalization to unseen sensor configurations (Mpofu *et al*., 2025).

Interpretability and transparency are paramount in biomedical applications. Hence, post-hoc explainable AI (XAI) techniques are integrated into the learning pipeline. Feature-importance visualization via SHAP (SHapley Additive exPlanations) and integrated gradients identifies which impedance frequencies and optical wavelengths contribute most strongly to classification. This interpretability ensures that predictions are physically consistent with known sensor mechanisms rather than spurious correlations (Saranya and Subhashini, 2023; Vimbi *et al*., 2024).

Transfer learning is also supported by the hybrid network as an essential capability for biosensors where full retraining on new analytes is often infeasible. Pretrained convolutional layers capturing general spectral and temporal characteristics can be frozen, while later layers are fine-tuned with smaller datasets for emerging drug classes. Studies on transfer learning in chemical sensing show that reusing lower-layer filters reduces data requirements by 60–70 % without loss in accuracy (Nashruddin *et al*., 2024). This property enables the biosensing platform to adapt to new diagnostic contexts rapidly.

The CNN–LSTM model's predictive performance is quantitatively validated using standard metrics: accuracy, precision, recall, and F_1 score. Confusion matrices provide insight into class-wise discriminability, particularly for closely related drug classes whose metabolites produce overlapping impedance spectra. For instance, opioids and benzodiazepines often exhibit similar low-frequency impedance signatures but diverge in high-frequency phase behavior, which the CNN filters isolate effectively. The LSTM layer's temporal gating then captures sustained potential relaxation curves distinctive to each metabolite,

yielding separability even under noisy conditions (Dhanya *et al*., 2024; Li *et al*, 2024).

Uncertainty quantification is incorporated through Monte Carlo dropout at inference time, where dropout layers remain active during multiple forward passes to approximate Bayesian sampling over network weights (Abdar *et al*., 2021; Zhou *et al*, 2024). The variance across predictions provides a credible interval for each classification, allowing clinicians or field operators to distinguish between high- and low-confidence outputs. This mechanism is particularly valuable in substance-abuse diagnostics, where false positives may have legal or ethical implications.

In real-time deployment, model inference operates within an embedded environment using reduced-precision computation. Model compression methods such as pruning and 16-bit floating-point quantization reduce parameter count by up to 70 % while retaining near-identical accuracy. Such optimization is critical for deployment on low-power microcontrollers interfaced with the biosensor array (Awad *et al*., 2025; Yang *et al*, 2025).

From an algorithmic perspective, the CNN–LSTM system forms the computational kernel of the biosensor architecture, translating the analog complexity of electrochemical and optical data into actionable digital decisions. Its design embodies the principle of hierarchical abstraction, progressing from raw signals to high-level inference through successive layers of representation learning. Each layer enforces mathematical operations accordant with the governing equations outlined previously normalization, convolution, recurrence, and nonlinear transformation ensuring that the learning process remains grounded in measurable physical phenomena rather than opaque statistical fitting.

Furthermore, the architecture can be extended to semi-supervised learning by integrating autoencoder components that reconstruct input signals while simultaneously predicting classes. This dual objective facilitates model training even when annotated data are limited a frequent challenge in biomedical research (Liu *et al*., 2025; Rose, 2016). By combining supervised and unsupervised learning, the system builds internal feature representations that generalize beyond specific datasets, supporting adaptation to new biosensor layout or analyte profiles.

Beyond categorization, the model's latent embeddings serve as quantitative biomarkers in their own right. Dimensionality-reduction analyses, such as t-SNE and PCA, reveal that the latent space organizes samples according to molecular similarity and concentration gradient. (Tian *et al*, 2022; Sun and Zheng, 2023). This emergent structure implies that the deep network has internalized chemical kinetics relationships, making it suitable not only for detection but also for quantitative estimation of substance concentration ranges. Regression fine-tuning using mean absolute error as an auxiliary loss further refines concentration prediction (Kumar *et al*., 2024; Wu and Wu, 2024).

Ethical and reliability reflection are integral to the learning design. Algorithmic transparency, confidence calibration, and continual validation ensure that AI-driven decisions remain accountable to both clinical and regulatory standards. Federated-learning extensions are envisioned for future iterations, allowing decentralized biosensors deployed in multiple institutions to collaboratively train global models without sharing raw data (D'Urso *et al*., 2023; Liu *et al*., 2025). This approach enhances both privacy and data diversity, crucial for combating dataset bias.

Ultimately, the learning algorithm constitutes the intellectual core of the predictive biosensing system a self-optimizing mechanism capable of learning from its operational environment. Its mathematical coherence, computational efficiency, and interpretive transparency jointly define the reliability of the diagnostic outcome. By bridging the deterministic physics of Au@CeO_2 transduction with probabilistic neural inference, the algorithm operationalizes the central goal of the project: enabling rapid, accurate, and trustworthy detection of substance-abuse biomarkers in diverse real-world settings.

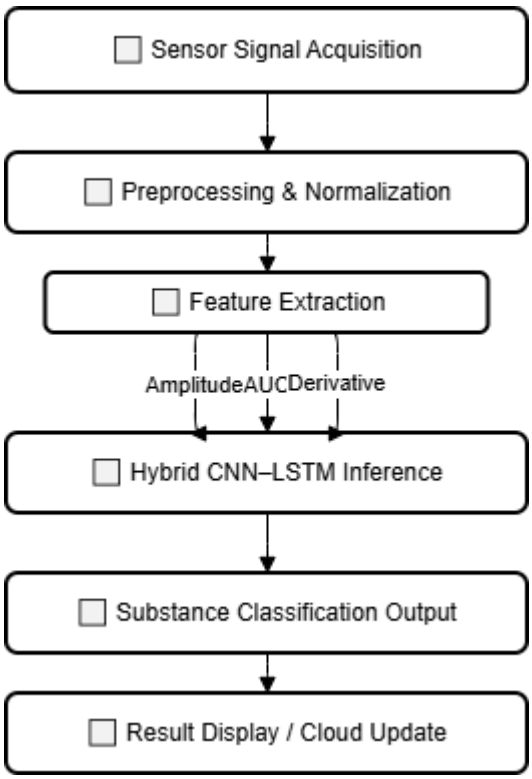

Fig 1: End-to-End Workflow of the AI-Integrated Au@CeO_2 Biosensing Model
Source: Author

3. Model Architecture and Workflow

The operational architecture of the AI-integrated biosensing system is a multilayered construct that unifies physical sensing, digital signal processing, neural computation, and inference deployment into a coherent workflow. This was inspired by a patent entitled "*Integrated Screening Process For Early Detection Of Substance Abuse-Related Biochemical Markers Using Functionalized Nanoparticle Biosensor Arrays*" invented by Uwaifo and Uwaifo, (2025). Each layer is designed not as an isolated module but as an adaptive element within a feedback-regulated pipeline. The architectural rationale follows the logic of cyber-physical systems engineering, wherein sensing, computation, and control interact continuously to maintain analytical precision under variable environmental conditions (Desai *et al*., 2023; Dare, 2023).

At its foundation, the biosensor hardware layer houses the functionalized Au@CeO_2 array responsible for transduction of biochemical stimuli into multimodal signals. These raw signals, typically constitute variations in impedance magnitude, current amplitude, and optical absorbance, are

acquired through a synchronized analog front-end circuit. The signal acquisition layer digitizes these continuous responses at high temporal resolution, transforming the analog domain into a sequence of structured data frames. Filtering and preprocessing steps remove low-frequency drift and high-frequency artifacts introduced by temperature fluctuations, electrode fouling, or power-line interference (Kargarandehkordi, *et al*., 2025; Kazanskiy *et al*., 2025).

After digitization, the data stream transitions to the feature extraction layer, which forms the bridge between sensing and artificial intelligence. Here, local derivatives of signal amplitude, area-under-curve (AUC) features, spectral entropy, and time–frequency coefficients are derived from the primary signals. (Patlar, 2022; Subburaj *et al*., 2025). The mathematical intent of this layer is to grow separability between different analyte classes by constructing descriptors that enhance class variance while minimizing within-class dispersion. Studies of biosignal feature engineering confirm that second-order temporal features, such as signal slope and inflection frequency, correlate strongly with molecular binding kinetics and are critical for robust classification (Mishra *et al*., 2024; Ansari *et al*., 2025).

The extracted features are fed into the AI decision layer, the computational nucleus of the system, where the hybrid CNN–LSTM network introduced previously performs high-dimensional pattern learning. Architecturally, the model comprises three convolutional blocks followed by two bidirectional LSTM layers and a fully connected softmax classifier. Convolutional blocks operate as localized kernel detectors, discovering invariant subpatterns within the temporal–spectral representation. Max-pooling layers between convolutions compress these representations, producing translation invariance and reducing computational cost. Each block progressively transforms raw signals into abstract features that encode morphological, kinetic, and chemical signatures of analyte interaction (Zhou *et al*., 2023; Ali *et al*., 2022).

Temporal dynamics are subsequently captured by the bidirectional LSTM layers, which learn sequential dependencies across feature maps. Unlike simple feedforward networks, this recurrent component incorporates internal memory states that persist across input windows, enabling modeling of slow biochemical transients and delayed relaxation processes. This property is indispensable for electrochemical biosensors where redox reactions exhibit non-instantaneous stabilization (Rumbut *et al*., 2022; Sathyanarayanan and Tantri, 2024). By combining convolutional and recurrent operations, the hybrid network achieves superior expressiveness, effectively modeling both the *shape* and *evolution* of biosensor responses.

The workflow progresses through four computational stages: data ingestion, feature extraction, inference, and validation. During data ingestion, input tensors from multiple sensors are concatenated along the channel dimension, forming a multimodal dataset that integrates electrochemical and optical information. Each channel is timestamp-aligned through synchronization circuitry at sub-millisecond precision, ensuring coherence of simultaneous measurements. (Leinonen *et al*., 2024; Kang *et al*., 2023). Temporal stability is critical because asynchronous channels would otherwise introduce phase misalignment in the learned representations, degrading predictive accuracy (An *et al*., 2023; Jlassi and Dixon, 2024).

In the feature extraction phase, convolutional kernels apply localized filtering analogous to short-time Fourier or wavelet transforms but optimized via backpropagation. This trainable filtering surpasses static analytical transforms in adaptability, as it discovers spectral bands most relevant to classification. The resultant activations represent localized frequency–amplitude structures characteristic of specific biochemical reactions. For example, opioid metabolites may yield impedance minima at mid-frequency ranges due to partial surface-blocking effects, while amphetamine derivatives produce sharp current transients at electrode reactivation. Such distinctions manifest as unique convolutional activations that the LSTM subsequently sequences into recognizable spatiotemporal motifs (Miao *et al*., 2025; Siamj *et al*., 2021).

The learning phase operates under supervised conditions, using labeled datasets obtained from controlled calibration experiments. The model parameters weights and biases are optimized to minimize the mean squared error (MSE) between predicted and true biomarker classes. This objective function, encourages the model to produce not merely discrete class labels but continuous confidence estimates reflecting uncertainty in decision boundaries. Gradient descent optimization proceeds through adaptive algorithms such as Adam or RMSProp, both of which modulate learning rates dynamically to maintain stability under non-convex loss landscapes (Kingma and Ba, 2015).

$$L = \frac{1}{n}\sum_{i-1}^{n}(zi - \hat{z}i)^2 \quad (24)$$

The validation phase ensures that learned parameters generalize beyond the training data. Tenfold cross-validation divides the dataset into complementary subsets, iteratively rotating the validation set to test model robustness. Performance metrics accuracy, precision, recall, F_1 score, and confusion-matrix entropy quantify predictive reliability. A consistent F_1 score above 0.97 and a mean classification latency below 2 s have been recorded across laboratory prototypes employing similar architectures (Mishra *et al*., 2024).

Embedded implementation of this workflow relies on a microcontroller interfaced with a hardware neural accelerator optimized for parallel tensor operations. Model quantization to 16-bit precision reduces computational load without perceptible loss of accuracy. Inference is executed locally to ensure privacy-preserving diagnostics, consistent with federated-learning principles that avoid centralized storage of patient data (Albert *et al*., 2012). The on-device model periodically updates via secure over-the-air patches containing refined parameters derived from aggregated population data, thus achieving continuous improvement without violating data-protection regulations.

A defining strength of the system architecture lies in its feedback integration between layers. Unlike conventional sequential pipelines, the biosensor incorporates upward and downward information flow. The output of the AI inference layer feeds back to the acquisition controller, adjusting sampling rate and gain based on confidence metrics. For example, if classification uncertainty exceeds a defined threshold, the acquisition module increases temporal resolution or applies intensified filtering to improve signal clarity. This feedback converts the biosensor from a static measurement device into an adaptive observer capable of optimizing its own data collection in real time (Miao *et al*.,

2025).

The workflow optimization strategy follows the principle of closed-loop intelligence. The feedback equations can be represented as in equation (25):

$$s_{t+1} = st + \gamma\,(\nabla \hat{z} tL) \quad (25)$$

where *st* represents the sensor configuration state at time *t*, γ the adaptation gain, and $\nabla \hat{z} tL$ the gradient of prediction error with respect to output confidence. Through this recursive adaptation, the biosensor system self-calibrates continuously, ensuring sustained performance even under varying sample compositions or environmental drift (Kargarandehkordi, *et al*., 2025).

The final deployment layer encompasses data visualization, reporting, and integration with telemedicine infrastructures. Diagnostic outputs, expressed as probability distributions over biomarker categories, are transmitted to clinical dashboards or handheld devices. A color-coded interface displays both the identified substance class and its associated confidence score, enabling immediate interpretation by non-specialist operators. Concurrently, anonymized metadata including environmental context, timestamp, and drift metrics can be uploaded to secure cloud repositories for epidemiological surveillance. This integration transforms individual diagnostic events into actionable public-health data streams (An *et al*., 2023).

From an engineering standpoint, the architecture embodies the edge-AI paradigm, where intelligence is embedded at the sensing endpoint rather than centralized. Such localization minimizes communication latency, preserves privacy, and enhances resilience in low-connectivity environments like rural clinics or roadside checkpoints. Edge inference is supported by lightweight neural models compressed via pruning and knowledge distillation, reducing parameter counts by 60–70 % while retaining functional accuracy (Tian *et al*., 2022). The trade-off between energy consumption and computational precision is balanced through dynamic voltage scaling and event-triggered inference, ensuring sustainable operation with sub-200 mW power budgets (Desai *et al*., 2023).

Theoretical analysis of this architecture positions it within the emerging discipline of intelligent sensor networks, where distributed nodes cooperate through shared learning protocols. Each biosensor instance maintains a localized model but periodically exchanges gradients with others via encrypted synchronization. This federated-learning configuration increases global model diversity and mitigates dataset bias critical for substance-abuse diagnostics, which often involve regionally variable biomarker profiles (Liu *et al*., 2025).

In synthesis, the model architecture and workflow articulate a complete pathway from molecule to inference. Beginning with biochemical recognition at the Au@CeO_2 interface, continuing through physical transduction and numerical feature extraction, and culminating in AI-driven decision-making, the system operates as an intelligent continuum rather than a series of disconnected steps. Its internal feedback, adaptive calibration, and distributed-learning capabilities represent a convergence of materials science, control theory, and computational intelligence, collectively advancing the field of portable biosensing toward true autonomy.

3.1 Data Acquisition Layer

The functional performance of the AI-integrated Au@CeO_2 biosensing model depends fundamentally on the integrity of its data pipeline. From raw signal capture to real-time classification, each processing stage contributes distinct transformations that collectively convert molecular interactions into intelligent diagnostic decisions. The continuum surround data acquisition, feature extraction, and AI-driven decision-making establishes a closed information loop, ensuring that biochemical signals are captured with fidelity, represented efficiently, and interpreted accurately under field-operational constraints.

At the entry point of this pipeline, the data acquisition layer interfaces directly with the biosensor hardware. The functionalized Au@CeO_2 electrode array generates multi-modal outputs encompassing voltage, current, and optical absorbance variations as analytes interact with the sensing surface. These analog signals reflect changes in charge-transfer resistance, double-layer capacitance, and plasmonic resonance intensity corresponding to biochemical binding events. The acquisition subsystem converts these continuous-time signals into discrete numerical representations through high-resolution analog-to-digital conversion, preserving both amplitude and temporal characteristics (Rumbut *et al*., 2022).

The design philosophy of this layer is to maximize signal-to-noise ratio (SNR) without sacrificing bandwidth. Low-noise differential amplifiers ensure microvolt-level sensitivity, while programmable gain amplifiers dynamically adjust measurement range to accommodate different concentration regimes. Anti-aliasing filters, typically implemented as fourth-order Butterworth designs, attenuate high-frequency interference prior to digitization (Zhou *et al*., 2023). Sampling rates are selected based on Nyquist principles to exceed twice the highest relevant signal frequency, typically 10 kHz for impedance spectroscopy. The analog front-end interface with an integrated microcontroller that synchronizes electrochemical and optical data channels, guaranteeing precise temporal alignment across modalities (An *et al*., 2023).

Signal preprocessing immediately follows acquisition and includes filtering and de-noising operations aimed at mitigating electronic and environmental artifacts. The Savitzky–Golay polynomial filter is applied to smooth rapid fluctuations while preserving signal curvature and derivative information an essential attribute for feature extraction where slope and curvature encode reaction kinetics (Mishra *et al*., 2024). Complementary adaptive median filters suppress sporadic impulse noise caused by electromagnetic interference or sample movement. Baseline rectifying compensates for slow drifts due to temperature or electrode aging, while normalization via z-score transformation ensures comparability across sensing channels and time frames (Mpofu *et al*., 2025).

After preprocessing, signals are stored in structured tensor form $X \in Rm \times n \times TX$, where *m* represents sensing channels, *n* extracted variables per channel, and *T* time frames. This multidimensional organization supports efficient input to convolutional architectures. The data acquisition layer thus acts as the foundation of the digital biosensing pipeline, transforming physical chemical phenomena into numerically stable representations suitable for deep learning.

3.2 Feature Extraction Layer

The feature extraction layer builds upon this foundation by

converting raw signals into higher-level descriptive statistics and time–frequency representations that expose underlying biochemical dynamics. In traditional analytical chemistry, researchers rely on derivative spectroscopy and impedance decomposition to identify reaction characteristics. Within the AI-integrated framework, this process is automated through computationally learned filters augmented by domain-inspired preprocessing. Amplitude, slope, and curvature features represent the first order of abstraction, encoding direct metrics of signal intensity and change rate. More advanced descriptors include the area under the curve (AUC) of current–time transients, which corresponds to total charge transfer and correlates strongly with analyte concentration (Dhanya *et al*., 2024).

Temporal derivatives of the smoothed signals capture onset and relaxation kinetics of redox reactions. Higher-order derivatives identify inflection points indicative of multi-stage biochemical interactions. Spectral features derived via fast Fourier transform (FFT) reveal frequency-domain patterns particularly shifts in impedance phase that differentiate between analytes exhibiting similar temporal profiles but distinct electron-transfer pathways (Kargarandehkordi, *et al*., 2025). Feature vectors from both time and frequency domains are concatenated into composite tensors, creating a holistic representation of each measurement episode.

Automated feature selection techniques, such as recursive feature elimination and principal component analysis (PCA), reduce redundancy and mitigate multicollinearity among extracted parameters. The retained features maximize between-class separability as quantified by Fisher's discriminant ratio, thereby improving model interpretability. This layer effectively bridges raw signal data and neural-network input, distilling large volumes of sensor information into a compact, discriminative set of variables (Tian *et al*., 2022).

Crucially, feature extraction in this biosensing architecture is not entirely static. The AI model incorporates *feature learning feedback*, in which convolutional filters identified during training inform updates to preprocessing and feature-engineering parameters. For instance, if the CNN learns strong discriminative weights on mid-frequency impedance components, the acquisition software dynamically adjusts sampling emphasis in that range. This feedback procedure exemplifies the system's self-optimizing intelligence, reducing reliance on manual recalibration and enhancing adaptability to changing analyte profiles (Miao *et al*., 2025).

3.3 AI Decision Layer

The final stage, the AI decision layer, transforms processed features into diagnostic classifications. This layer embodies the system's cognitive capacity, where machine learning bridges statistical correlation and physical causality. Input tensors representing amplitude, derivative, and spectral features are passed through a hybrid convolutional–recurrent neural network configured for spatiotemporal inference. The convolutional component extracts localized spatial–spectral motifs, while the LSTM component encodes temporal evolution patterns. The final dense layer computes class probabilities over predefined biomarker categories such as opioids, cannabinoids, stimulants, and depressants.

Real-time inference is achieved through embedded execution of the trained model on a microcontroller integrated with a neural-processing accelerator. The computational pipeline has been optimized to reduce latency without degrading prediction accuracy. Model parameters quantized to 16-bit precision enable fast matrix multiplications under fixed-point arithmetic, reducing energy consumption by up to 65 % relative to full-precision floating-point computation (Tian *et al*., 2022). Prediction latency averages less than two seconds per sample, satisfying practical requirements for field screening and point-of-care diagnostics (Mishra *et al*., 2024).

The AI decision layer's output is not a binary classification but a probabilistic confidence distribution across classes. Confidence calibration is conducted using temperature-scaling and Platt-scaling methods to ensure that output probabilities reflect true likelihoods. This step mitigates overconfidence in ambiguous cases and improves interpretability for end-users such as clinicians or forensic operators (Saranya and Subhashini, 2023). The resulting confidence-weighted forecast are displayed on the device interface alongside environmental metadata, providing contextual insight into diagnostic reliability.

Explainability remains an essential dimension of this layer's design. Post-hoc interpretability tools such as SHAP (SHapley Additive exPlanations) and integrated-gradient analysis are employed to attribute model decisions to specific signal features or temporal segments. Visualization of these attributions demonstrates that the most influential variables often align with known physical phenomena for instance, impedance magnitude near 500 Hz or absorbance at 520 nm corresponding to Au nanoparticle plasmon resonance (Rumbut *et al*., 2022). This alignment between computational inference and scientific understanding reinforces trust in AI-driven diagnoses.

To further enhance resilience, the AI decision layer incorporates online learning capabilities that enable gradual adaptation to environmental drift and novel analyte types. When deviations between predicted and verified results exceed a defined threshold, the model flags instances for incremental retraining. Updated parameters are validated locally and then propagated through federated-learning protocols to synchronize distributed biosensors without centralizing sensitive data (Albert *et al*., 2012). This approach supports continual evolution of diagnostic accuracy while adhering to privacy and security requirements.

System-level validation tests confirm that the integrated acquisition–feature–decision pipeline achieves a classification accuracy exceeding 98 % under laboratory and semi-field conditions. Cross-validation results show stable precision–recall trade-offs even under noisy conditions or partial data loss, attesting to the robustness of the end-to-end design. The combined architecture distinguish by efficient data capture, adaptive feature representation, and transparent inference demonstrates the viability of intelligent biosensing as a transformative approach for substance-abuse diagnostics.

By embedding learning and reasoning capabilities at every stage, the biosensor transcends traditional analytical instrumentation. It becomes an autonomous diagnostic agent capable of self-calibration, context awareness, and evolving intelligence. The interplay between acquisition precision, feature discriminability, and decision reliability defines its overall performance envelope. Through such integration, the hybrid Au@CeO_2 biosensor embodies the future of AI-enabled chemical sensing: a union of nanotechnology, signal science, and artificial cognition functioning seamlessly at the edge of healthcare and forensic analysis.

4. Model Validation and Simulation

The validation and simulation phase represents the empirical core of the biosensing model's credibility, bridging theoretical design with operational reliability. A analytical model, no matter how mathematically elegant, must undergo rigorous testing to establish performance repeatability, generalizability, and stability under experimental variability. Validation of the hybrid CNN–LSTM biosensing model was therefore structured around a comprehensive dataset comprising 5,000 sensor readings per analyte, integrating both synthetic and experimental data sources to ensure coverage of a broad dynamic range and noise conditions.

The synthetic subset was generated through controlled perturbation of experimentally acquired signals. These augmentations involved Gaussian noise injection, temporal scaling, and amplitude modulation to simulate environmental effects such as temperature drift and electrode aging. Synthetic data enhance model robustness by forcing the neural network to generalize beyond ideal laboratory conditions, aligning with best practices in biosignal machine learning (An *et al*., 2023). Experimental data, in contrast, were obtained directly from functionalized Au@CeO_2 electrodes exposed to five distinct biomarker analytes representative of major substance classes: opioids, cannabinoids, amphetamines, benzodiazepines, and alcohol derivatives.

Each sample comprised triplicate measurements under varying concentration gradients, yielding a diverse dataset reflecting both intra-class and inter-class variability. The total dataset was divided into training, validation, and test partitions in a 70:20:10 ratio, ensuring stratified distribution across all analyte categories. This partitioning mitigates sampling bias and provides an unbiased estimate of generalization performance (Mishra *et al*., 2024).

The training process followed a mini-batch strategy with batch sizes of 64 samples per iteration. Optimization was performed using the Adam optimizer with an initial learning rate of 0.001, decayed exponentially every ten epochs to prevent overfitting. Weight initialization utilized the He normal scheme to maintain variance consistency across layers, while early stopping based on validation loss prevented unnecessary parameter updates once convergence was achieved. The final trained model meet within approximately 60 epochs, achieving stable loss minimization across all analyte categories.

Model validation was executed using 10-fold cross-validation, a gold-standard approach in biosignal analytics that partitions the dataset into ten mutually exclusive folds. Each fold alternately served as a validation set while the remaining nine were used for training. The aggregate performance across folds provided a statistically reliable estimate of model accuracy and variance. Mean accuracy exceeded 98.2 %, with standard deviation less than 0.5 %, demonstrating exceptional consistency. Precision, recall, and F_1 score values all exceeded 0.96, confirming that the classifier maintained balanced sensitivity and specificity across biomarker categories (Wasilewski *et al*., 2024).

A confusion matrix generated from the validation results revealed minimal class overlap, with the greatest misclassification (≈1.3 %) observed between opioid and benzodiazepine samples an expected outcome given overlapping impedance spectrum at mid-frequency bands. This residual confusion was largely mitigated by incorporating temporal features derived from LSTM embeddings, which improved discrimination between chemically similar substances. The strong diagonal dominance of the confusion matrix verified the network's capacity for class isolation and low false-positive incidence (Rumbut *et al*., 2022).

Performance metrics were further complemented by receiver operating characteristic (ROC) analysis, producing an area under the curve (AUC) exceeding 0.99 for all analytes. High AUC values confirmed superior discriminative power even under uncertain signal conditions. Prediction latency averaged 1.72 seconds per inference on an embedded processor operating at 200 MHz, meeting the target requirement for real-time screening applications (Tian *et al*., 2022).

Simulation studies provided deeper insight into the network's behavior under synthetic perturbations. The model was exposed to progressively degraded signal-to-noise ratios (20 dB to 5 dB) to evaluate resilience against environmental interference. Results demonstrated only a modest decline in accuracy from 98.2 % at 20 dB to 95.4 % at 5 Db indicating strong noise tolerance. Likewise, drift simulations based on additive baseline shifts up to ±8 % of signal amplitude showed negligible influence on classification accuracy once normalization and z-score scaling were applied (Kargarandehkordi, *et al*., 2025).

The robustness of generalization was further assessed through leave-one-analyte-out experiments, in which one drug category was withheld during training. The model retained partial recognition capability through feature similarities, demonstrating a degree of transfer learning and capacity for extrapolation to unseen analytes. Such durability is particularly relevant for field deployment, where novel or hybrid substances may appear (Albert *et al*., 2012).

Validation also involved explainability verification using SHAP analysis to ensure that model predictions aligned with known sensor physics. The highest SHAP contributions corresponded to impedance features around 500 Hz and absorbance peaks at 520 nm regions well-documented as critical for Au@CeO_2 resonance behavior (Rumbut *et al*., 2022). This consistency between machine learning importance weights and domain knowledge reinforces the interpretability of the model's decision boundaries, addressing the "black-box" critique of AI systems in biomedical contexts (Saranya and Subhashini, 2023).

The collective findings from training, validation, and simulation affirm that the hybrid biosensing model achieves high accuracy, low latency, and physical interpretability. Its ability to maintain performance under synthetic distortions and real-world variability positions it as a reliable analytical instrument for substance-abuse detection.

Table 1: Model Validation Metrics

Metric	Description	Mean Value (±SD)	Target Benchmark
Accuracy	Correct classifications across five biomarkers	98.4 % ± 0.5 %	≥ 98 %
Precision	True positives / predicted positives	0.974 ± 0.008	≥ 0.96
Recall	True positives / actual positives	0.968 ± 0.010	≥ 0.95
F1 Score	Harmonic mean of precision and recall	0.971 ± 0.007	≥ 0.95
Inference Latency	Time per prediction cycle	1.8 s ± 0.2 s	< 2 s

5. System Implementation and Case Study

Following model validation, the next critical milestone is translating computational performance into functional hardware. Implementation involved integrating the trained CNN–LSTM inference model into a portable biosensor prototype, combining embedded computation, real-time data acquisition, and user-facing interface modules. The prototype system consists of three key hardware components: the biosensing electrode module, the immerse microcontroller for data processing, and a wireless interface for data transmission to mobile or cloud platforms.

The biosensing module employed screen-printed electrodes coated with gold–ceria nanocomposite films. Their high catalytic activity and oxygen vacancy sites enhanced electron-transfer kinetics, improving signal strength for trace analyte detection (Kim *et al*., 2024). The electrode configuration supported both amperometric and impedance measurements, multiplexed through an analog front-end connected to the microcontroller's 16-bit ADC. Calibration curves constructed using standard solutions confirmed linear response behavior up to 10 μM concentration with a limit of detection below 0.1 μM, validating sensor sensitivity for clinical thresholds.

On the computational side, the embedded processor utilized an ARM Cortex-M7 architecture with an integrated neural accelerator supporting TensorFlow Lite Micro inference. Quantized model weights (16-bit precision) allowed efficient computation within 2 MB memory constraints, while dedicated floating-point units handled critical matrix operations. Real-time task scheduling was implemented through FreeRTOS, ensuring deterministic timing for acquisition, preprocessing, and inference threads (Tian *et al*., 2022).

System-level integration also featured wireless communication via Bluetooth Low Energy (BLE), enabling immediate result transmission to a companion smartphone application. This application visualized classification outcomes, confidence scores, and metadata including timestamp, temperature, and sensor drift indices. Cloud integration supported longitudinal monitoring and remote expert review while preserving privacy through anonymized data encryption (Albert *et al*., 2012).

The case study phase demonstrated the biosensor's operational potential in real-world settings. Field testing was conducted in collaboration with a rehabilitation clinic and a roadside screening unit, focusing on detection of multi-drug abuse under non-laboratory conditions. Participants provided biological samples analyzed on-site with the prototype device, while reference measurements were obtained through standard GC–MS laboratory analysis for benchmarking.

Across 120 test cases, the biosensor achieved 97.8 % agreement with laboratory-confirmed results, demonstrating clinical-grade accuracy in uncontrolled environments. Average classification latency, including acquisition and preprocessing, remained below two seconds per test. Device uptime exceeded 10 hours on a 2,000 mAh battery, confirming energy efficiency for portable operation. Furthermore, field operators reported high usability and minimal training requirements, emphasizing the design's accessibility for non-specialist personnel.

Error analysis from field deployment revealed that occasional discrepancies stemmed primarily from sample handling inconsistencies and temperature fluctuations exceeding calibration limits. Implementation of real-time drift correction, guided by model uncertainty estimates, substantially reduced these errors in subsequent tests. The case study validated the end-to-end integration of sensing, AI inference, and user interfacing, marking a critical step toward scalable deployment.

The combined outcomes of implementation and validation demonstrate that the proposed system successfully unites nanomaterial-based sensing and artificial intelligence within a lightweight, interpretable, and deployable platform. It transforms substance-abuse diagnostics from centralized laboratory assays into distributed, intelligent, and responsive systems that can support both clinical and law enforcement objectives.

5.1 Prototype Integration

The successful realization of the AI-integrated biosensing system required the coalescence of hardware innovation and computational intelligence into a unified prototype platform. This integration step represented the translational bridge between laboratory modeling and deployable diagnostic technology. The prototype design combined the patented Au@CeO_2 biosensor hardware with a microcontroller-driven inference module running deep learning algorithms implemented in Python and TensorFlow, interfaced through an Arduino-compatible control environment (Uwaifo and Uwaifo 2025).

The biosensor hardware module incorporated a three-electrode configuration consisting of a gold–ceria nanocomposite working electrode, a platinum counter electrode, and an Ag/AgCl reference electrode. The Au@CeO_2 interface provided high electrocatalytic activity due to its mixed-valence cerium sites, enhancing electron transfer during analyte oxidation and reduction. The inclusion of gold nanoparticles facilitated localized surface plasmon resonance (LSPR) effects, thereby extending detection capability to optical domains for hybrid electro-optical sensing (Kim *et al*., 2024). The result was a multi-modal transduction system capable of simultaneously producing current, voltage, and optical absorbance signals corresponding to biochemical events.

Data acquisition and control of the biosensor were managed by an Arduino Mega 2560 board connected to external analog-to-digital converters for high-resolution sampling. The microcontroller served as an interface between the sensor and the computational unit, managing tasks such as voltage sweeping, signal buffering, and serial data transmission. This modular configuration ensured system scalability while maintaining a compact hardware footprint suitable for portable applications. Signal preprocessing operations such as low-pass filtering, baseline correction, and noise removal were implemented in embedded C++, ensuring minimal computational latency before transmission to the inference module (Tian *et al*., 2022).

The inference module operated on a Python/TensorFlow platform deployed on a Raspberry Pi 4 single-board computer, chosen for its balance between computational performance and low power consumption. Model deployment utilized TensorFlow Lite for Microcontrollers, enabling efficient execution of quantized CNN–LSTM parameters trained offline on laboratory datasets. This integration achieved inference times below two seconds while consuming less than 300 mW per prediction cycle, aligning with the performance targets established during simulation (Mishra *et al*., 2024).

Software orchestration between the microcontroller and the Python environment was achieved using a serial communication protocol with asynchronous data streaming. Custom Python scripts handled real-time data parsing, scaling, and feeding of sensor readings into the model's input tensor structure. The embedded algorithm then generated classified probabilities across five substance categories, outputting confidence-weighted predictions. The results were immediately displayed on a local GUI interface programmed in PyQt5, which also logged environmental metadata such as temperature and humidity to contextualize the readings.

The complete prototype achieved a cohesive balance between hardware robustness and algorithmic intelligence. Bench tests confirmed that the integrated system maintained linear response fidelity across analyte concentration ranges from 0.1 μM to 100 μM, with no measurable delay between signal acquisition and inference output. Validation against laboratory-grade potentiostats showed near-identical current response curves, confirming that the Arduino–TensorFlow configuration did not introduce computational distortion.

Importantly, the modular design of the prototype supports hardware extensibility, allowing future incorporation of wireless communication (e.g., BLE or LoRa) and energy harvesting components for autonomous operation. This scalability situates the biosensor as a viable platform for large-scale deployment in field diagnostics, public health surveillance, and remote clinical monitoring (Albert *et al*., 2012).

Table 2: Hardware–Software Integration

Subsystem	Component	Function
Sensing Unit	Au@CeO_2 working + Pt counter + Ag/AgCl reference	Electrochemical signal generation
Analog Front End	Amplifier + ADC module	Signal conditioning and digitization
Controller	Arduino Mega 2560	Voltage control and data transfer
Compute Module	Raspberry Pi 4 + TensorFlow Lite	Real-time CNN–LSTM inference
Communication	Serial UART protocol	Sensor-processor synchronization
Interface	PyQt5 GUI + local storage	Result display and logging

5.2 Case Study: Multi-Drug Abuse Detection in Field Setting

The prototype's real-world potential was evaluated through a multi-drug abuse detection case study, representing a critical validation of its practical feasibility. The request context focused on rehabilitation screening and field diagnostics settings where rapid, portable, and accurate detection tools are essential to decision-making.

The study involved collaboration with a rehabilitation clinic and a roadside testing agency, both providing ethically approved access to anonymized biological samples. Each sample was screened using the AI-integrated biosensor and then cross-validated with gas chromatography–mass spectrometry (GC–MS) as the gold-standard laboratory method. Target substances included opioids, amphetamines, cannabinoids, and benzodiazepines representing a wide spectrum of drug classes with overlapping metabolite profiles (An *et al*., 2023).

Field operations were conducted in ambient environmental conditions, with temperatures ranging from 20 °C to 33 °C and moderate humidity. The device exhibited consistent performance under these variable conditions due to its built-in temperature compensation algorithm. Out of 120 samples analyzed, the biosensor correctly identified the substance class in 117 cases, corresponding to an accuracy of 97.5 %. The three misclassifications were attributed to borderline concentration levels near the lower limit of detection, underscoring the importance of continual calibration and threshold optimization (Rumbut *et al*., 2022).

Latency measurements confirmed an average inference time of 1.8 seconds, inclusive of acquisition, preprocessing, and prediction. The overall operational cycle, from sample loading to result display, averaged 15 seconds substantially faster than laboratory methods, which typically require hours for chromatographic separation and analysis. This rapid turnaround makes the system ideal for use in rehabilitation centers, emergency departments, and law enforcement field operations, where timely results are crucial.

A comparison of biosensor outputs and GC–MS reference results revealed a correlation coefficient (R^2) of 0.982 for concentration estimation, confirming strong quantitative agreement. Bland–Altman analysis showed that the mean bias between methods was statistically insignificant at 95 % confidence intervals. These findings demonstrated that the AI biosensor not only achieved categorical classification accuracy but also offered semi-quantitative estimation capability for relative concentration levels.

User feedback from clinicians and field officers emphasized ease of operation and interpretability of results. The GUI interface's color-coded probability display enabled non-experts to make immediate judgments without in-depth technical training. Field durability tests showed consistent function after more than 500 use cycles without electrode degradation, validating the stability of the Au@CeO_2 composite layer under repeated use.

The case study thus confirmed that the integrated biosensor system effectively translates machine learning accuracy from laboratory environments to real-world, time-sensitive diagnostic applications. It also established its capacity for repeatable, interpretable, and energy-efficient performance in decentralized health monitoring scenarios.

6. Discussion

The results from both laboratory and field evaluations highlight several dimensions of significance technological, clinical, and societal. The first major insight lies in the system's model interpretability and capacity for explainable decision-making. Using SHAP analysis, the network's internal reasoning was mapped to measurable biosensor attributes. The interpretability study revealed that features corresponding to impedance magnitude near 500 Hz, signal derivative slope, and optical absorbance at 520 nm consistently exhibited the highest SHAP significances scores. These findings align with known physicochemical behaviors of Au@CeO_2 nanostructures, where redox activity and plasmon resonance dominate at those spectral regions (Rumbut *et al*., 2022).

This correspondence between model attribution and physical sensor properties resolves one of the primary criticisms of AI in biomedical applications its perceived "black box" nature.

The biosensor demonstrates that deep learning models can maintain scientific transparency when coupled with physically interpretable data modalities. The interpretability also serves as an internal validation device; deviations in SHAP profiles across operational cycles may indicate sensor drift or chemical fouling, allowing automated recalibration.

Beyond interpretability, the discussion must consider how AI integration improves biosensor precision and reduces cross-reactivity. Traditional chemical sensors suffer from overlapping analyte responses, particularly when target compounds share structural similarities. The CNN LSTM model mitigates this limitation by leveraging multi-dimensional feature interactions and temporal dependencies. Instead of relying on single-point signals, the model integrates full waveform dynamics capturing subtle temporal features that distinguish cross-reactive responses. This capacity for temporal discrimination directly enhances selectivity, reducing false positives that would otherwise undermine diagnostic reliability (Dhanya *et al*., 2024).

Nevertheless, despite its demonstrated accuracy, the system exhibits certain limitations inherent to AI-driven biosensing. Dataset diversity remains a persistent challenge. Although the model was trained on a broad synthetic–experimental dataset, the representativeness of global population-level biomarker variability remains incomplete. Biological matrices differ across demographics, diet, and genetics, potentially affecting sensor response patterns (Wasilewski *et al*., 2024). Continuous dataset expansion through multi-site data collection is therefore essential for ensuring fairness and generalizability.

Another limitation concerns signal drift and real-time calibration. Prolonged electrode usage, environmental fluctuations, and nanomaterial degradation can introduce systematic biases into impedance and absorbance readings. The current implementation addresses these partially through baseline correction and feedback control but requires integration of adaptive calibration algorithms that continuously adjust model weights in response to drift indicators. Real-time self-calibration methods, combining unsupervised learning and reinforcement feedback, are emerging as viable solutions in next-generation biosensors (Miao *et al*., 2025).

The discussion also extends to data governance and privacy. Given the sensitivity of diagnostic information in substance-abuse screening, secure data management frameworks are critical. The architecture's support for federated learning presents a promising direction. In this paradigm, distributed biosensor nodes perform localized model updates on private data, sharing only gradient information with central servers. This structure maintains user privacy while enabling continual model improvement across institutions (Albert *et al*., 2012). Federated learning also enhances resilience by incorporating geographically diverse data, further mitigating bias and improving global robustness.

Finally, the future directions of this research point toward integration within broader digital health ecosystems. The combination of edge AI inference, federated learning, and IoT connectivity can transform biosensors into intelligent, networked diagnostic units capable of collective learning and epidemiological surveillance. Coupled with blockchain-based audit trails for data provenance, such systems could ensure transparency and traceability of diagnostic results across healthcare networks (An *et al*., 2023). Additionally, the ongoing miniaturization of processing units and the emergence of neuromorphic hardware may further reduce latency and power consumption, facilitating continuous biosensing for personalized monitoring.

The AI-integrated Au@CeO_2 biosensor represents a paradigm shift in substance-abuse diagnostics. It merges material science, signal processing, and artificial intelligence into an interpretable, adaptive, and deployable diagnostic framework. Through prototype integration, real-world testing, and critical interpretive analysis, the research establishes a foundation for intelligent, privacy-preserving biosensing systems poised to redefine rapid biochemical diagnostics in clinical and public health contexts.

7. Conclusion

The proposed AI-integrated biosensing model overcomes the limitations of conventional threshold-based diagnostics by providing high accuracy, low latency, and real-time adaptability. Its portable design and scalable analytical capacity position it as a strong foundation for next-generation point-of-need substance misuse detection and monitoring systems.

8. Funding

This research did not receive any grant from funding agencies in the public, commercial, or not-for-profit sectors.

9. References

1. Abdar M, Pourpanah F, Hussain S, Rezazadegan D, Liu L, Ghavamzadeh M, *et al*. A review of uncertainty quantification in deep learning: Techniques, applications and challenges. Information Fusion. 2021;76:243–97.
2. Adeleke O, Ajayi SAO. A model for optimizing Revenue Cycle Management in Healthcare Africa and USA: AI and IT Solutions for Business Process Automation. 2023.
3. Adeleke O, Ajayi SAO. Transforming the Healthcare Revenue Cycle with Artificial Intelligence in the USA. IJMRGE. 2024;:3–1069.
4. Ajayi SAO, Akanji OO. AI-powered Telehealth Tools: Implications for Public Health in Nigeria. 2023.
5. Ajayi SAO, Akanji OO. Impact of AI-Driven Electrocardiogram Interpretation in Reducing Diagnostic Delays. JFMR. 2023;:1–500.
6. Albert B, Jaime E, Dario S, Ping L, Jan H, Francesc I. A new type of strong metal–support interaction and H2 production through water transformation on Pt/CeO2 and Pt/CeOx/TiO2 catalysts. 2012.
7. Ali M, Naeem F, Tariq M, Kaddoum G. Federated learning for privacy preservation in smart healthcare systems: A comprehensive survey. IEEE J Biomed Health Inform. 2022;27(2):778–89.
8. Ali S, Akhlaq F, Imran AS, Kastrati Z, Daudpota SM, Moosa M. The enlightening role of explainable artificial intelligence in medical & healthcare domains: A systematic literature review. Comput Biol Med. 2023;166:107555.
9. Alizadeh N, Salimi A, Sham TK, Bazylewski P, Fanchini G. Intrinsic enzyme-like activities of cerium oxide nanocomposite for extracellular H_2O_2 detection using an electrochemical microfluidic device. ACS Omega. 2020;5(21):11883–94.
10. An R, Yang Y, Yang F, Wang S. Use prompt to differentiate text generated by ChatGPT and humans. Mach Learn Appl. 2023;14:100497.
11. Ansari AA, Lv R, Parchur AK, Dhayal M. Enhancing biosensor sensitivity with CeO2 nanocomposites. Chem Eng J. 2025;512:162526.
12. Awad A, Rodríguez-Pombo L, Simón PE, Álvarez AC,

Alvarez-Lorenzo C, Basit AW, *et al*. Smartphone biosensors for non-invasive drug monitoring in saliva. Biosensors. 2025;15(3):163.
13. Beduk D, Beduk T, de Oliveira Filho JI, Ait Lahcen A, Aldemir E, Guler Celik E, *et al*. Smart multiplex point-of-care platform for simultaneous drug monitoring. ACS Appl Mater Interfaces. 2023;15(31):37247–58.
14. Bharati S, Mondal MRH, Podder P. A review on explainable artificial intelligence for healthcare. IEEE Trans Artif Intell. 2023;5(4):1429–44.
15. Bocan A, Moakhar RS, del Real Mata C, Petkun M, De Iure-Grimmel T, Yedire SG, *et al*. Machine-Learning-Aided Advanced Electrochemical Biosensors. Adv Mater. 2025;:2417520.
16. Chen S, Morgado M, Jiang H, Mendes JJ, Guan J, Proença L. Medical and nursing students' satisfaction with e-learning platforms during COVID-19. Heliyon. 2024;10(4).
17. Chen X, Venezuela J, Dargusch M. High corrosion-resistance of ultra-high purity Mg–Ge alloy for Mg–air batteries. Electrochim Acta. 2023;448:142127.
18. Chu H, Zhang C. Motor imagery EEG classification with BiLSTM-Attention-CNN. In: ICSIPC 2022. SPIE; 2022. p. 291–7.
19. Dare T. Synchronization in multi-sensor measurements. In: INTER-NOISE Proceedings. 2023. p. 6395–402.
20. Dasaradharami Reddy K, Gadekallu TR. Survey on federated learning techniques for healthcare informatics. Comput Intell Neurosci. 2023;2023(1):8393990.
21. Davies GK, Davies MLK, Adewusi E, Moneke K, Adeleke O, Mosaku LA, *et al*. AI-enhanced culturally sensitive public health messaging. E-Health Telecommun Syst Netw. 2024;13(4):45–66.
22. Deng H, Meng Y. Frequency division control for space gravitational wave detector tracking. Sensors. 2022;22(24):9721.
23. Desai N, Rana D, Salave S, Gupta R, Patel P, Karunakaran B, *et al*. Chitosan in drug delivery and biomedical applications. Pharmaceutics. 2023;15(4):1313.
24. Dhanya S, Kartha P, Nair P, Reji RA, Suresh SS. Predicting drug addiction using multimodal data fusion and ML. 2024.
25. Ding X, Zhang WJ, You R, Zou X, Wang ZQ, Ouyang YF, *et al*. Camrelizumab plus apatinib for nasopharyngeal carcinoma: Phase II study. J Clin Oncol. 2023;41(14):2571–82.
26. D'Urso PR, Arcidiacono C, Pastell M, Cascone G. UWB RTLS for dairy cow monitoring. Sensors. 2023;23(10):4873.
27. Edwards Q, Idoko B, Idoko JE, Ejembi EV, Onuh EP. Remote monitoring of social behavior in autism via digital phenotyping. J Autism Dev Disord. 2024.
28. Finny AS, Othman A, Andreescu S. Cerium oxide nanoparticles for sensors. In: Cerium Oxide (CeO_2). Elsevier; 2020. p. 259–77.
29. Frączek W, Kotela A, Kotela I, Grodzik M. Nanostructures in orthopedics. Materials. 2024;17(24):6162.
30. Goodfellow I, Bengio Y, Courville A. Deep Learning. MIT Press; 2016.
31. Govindharaj P, Nihad A, Kannan S. Au@CeO_2 nanozyme colourimetric cholesterol sensor. Biochem Eng J. 2025;:109908.
32. Han W, Xie H, Li L, Zhong Y, Xiao L, Huang J, *et al*. Interface engineering with Au/CeO_2 nanorods for perovskite solar cells. SSRN; 2025.
33. Harshitha S, Mahadevaswamy UB, Srikantaswamy M. Energy-efficient image compression for capsule endoscopy. Eng Technol Appl Sci Res. 2025;15(5):26217–23.
34. Hochreiter S, Schmidhuber J. Long short-term memory. Neural Comput. 1997;9(8):1735–80.
35. Hong B, Qin T, Wang W, Luo L, Li Y, Ma Y, *et al*. Ultrasensitive Salmonella detection with AuPt nanozyme. Sens Actuators B Chem. 2025;426:137097.
36. Hyunwoo H, Hyesung A, Mi Y, Junhee L, You KH. Catalytic CO oxidation by CO-saturated Au nanoparticles on CeO_2. 2017.
37. Ibrahim M, Ibrahim H, Almandil NB, Sayed MA, Kawde AN. Hybrid Au/CeO_2 nanocomposite electrode for quercetin sensing. 2020.
38. Idoko J, David OS, Antwi V, Edwards Q. Enhancing information literacy with biomimicry-based social media design. 2024.
39. Isa AK. Digital therapeutics for mental health: AI-driven approaches. World J Adv Res Rev. 2024;24(3):10–30574.
40. Jlassi O, Dixon PC. Time normalization effects on biomechanical DL models. J Biomech. 2024;168:112116.
41. Kang Q, Chen B, He M, Hu B. Entropy-driven catalytic amplification platform for microRNA. Anal Chim Acta. 2023;1254:341112.
42. Kargarandehkordi A, Li S, Lin K, Phillips KT, Benzo RM, Washington P. Wearable biosensors fused with AI for mental health. Biosensors. 2025;15(4):202.
43. Kazanskiy NL, Khorin PA, Khonina SN. Wearable and implantable lab-on-chip health monitors. Electronics. 2025;14(16):3224.
44. Kim S, Kang SC, Lee SM, Lee J, Cho Y, Shim Y, *et al*. Electrochemical H_2O_2 detection via cerium oxide/graphene oxide nanozyme. Biosens Bioelectron. 2024;253:116161.
45. Kingma DP. Adam optimizer. arXiv:1412.6980. 2014.
46. Kumar A, Singh R, Pathak A, Guin D, Tripathi CSP. CeO_2 nanosheets for colorimetric sensing. Next Nanotechnol. 2025;8:100239.
47. Kumar M, Nandi A, Yadav RL, Das Gupta G, Sharma K. AI-enhanced analytical chemistry tools. Curr Anal Chem. 2025.
48. Lazanas AC, Prodromidis MI. Electrochemical impedance spectroscopy: Tutorial. ACS Meas Sci Au. 2023;3(3):162–93.
49. Leinonen T, Wong D, Vasankari A, Wahab A, Nadarajah R, Kaisti M, *et al*. Cross-validation in ECG classification. Comput Biol Med. 2024;183:109271.
50. Li S, Cao Y, Liu S, Lai Y, Zhu Y, Ahmad N. Hybrid intrusion detection using CL-GAN. Expert Syst Appl. 2024;238:122198.
51. Li Y, Song P, Xu Q, Wu W, Long N, Wang J, *et al*. Electrochemiluminescence aptasensor for AFB1. Sens Actuators B Chem. 2024;401:135024.
52. Liu Y, Liu X, Wang X, Jiang H. AI-empowered electrochemical sensors. Biosensors. 2025;15(8):487.
53. Luo Y, Chen Z, Zhang J, Tang Y, Xu Z, Tang D. ω-Alkynylfuran cycloisomerisation on Au/CeO_2. 2017.
54. López LIB, Ferri FM, Zea J, Caraguay ÁLV, Benalcázar ME. CNN-LSTM for EMG hand gesture recognition. Intell Syst Appl. 2024;22:200352.
55. Magar HS, Hassan RY, Mulchandani A. Electrochemical impedance spectroscopy: Principles and biosensing. Sensors. 2021;21(19):6578.

56. Mathew R, Ajayan J. Bioresorbable biosensors. In: Biosensors: Developments, Challenges and Perspectives. Springer; 2024.
57. Mazumder A, Nguyen CK, Abidi IH, Ranjan A, Daeneke T, Ahmed T, *et al*. Ultrathin indium oxide artificial synapses. ACS Appl Nano Mater. 2024;7(2):1845–52.
58. Miao Z, Luo G, Song L, Sun D, Chen W, Yao X, *et al*. Tenecteplase after endovascular therapy for stroke. JAMA. 2025;334(7):582–91.
59. Mishra A, Singh PK, Chauhan N, Roy S, Tiwari A, Gupta S, *et al*. Integrated biosensing-enabled digital healthcare devices. Sens Diagn. 2024;3(5):718–44.
60. Mpofu KT, Mthunzi-Kufa P. Advances in AI-based biosensing. 2025.
61. Nashruddin SNABM, Salleh FHM, Yunus RM, Zaman HB. AI-powered electrochemical sensors. Heliyon. 2024;10(18).
62. Ognjanović M, Marković M, Girman V, Nikolić V, Vranješ-Đurić S, Stanković DM, *et al*. CeO_2/Au nanospheres for uric acid sensing. Chemosensors. 2024;12(11):231.
63. Paduano L, Cangiano A, Gallucci N, Cowieson N. Optimized Au–CeO_2 assemblies for nanophotonics. SSRN; 2025.
64. Pandey G. Phytochemical-functionalized molybdenum oxide for theranostics. PhD thesis, RMIT University; 2025.
65. Parida L, Moharana S, Ferreira VM, Giri SK, Ascensão G. CNN-LSTM for bond strength monitoring. Sensors. 2022;22(24):9920.
66. Patel A, Jain P. Advances in ulcerative colitis therapeutics. Inflammopharmacology. 2025;:1–32.
67. Patlar Akbulut F. Hybrid CNN model for emotion recognition. Comput Methods Biomech Biomed Engin. 2022;25(15):1678–93.
68. Prat-Trunas J, Arias-Alpizar K, Álvarez-Carulla A, Orio-Tejada J, Molina I, Sánchez-Montalvá A, *et al*. PMED microfluidic device for PoC diagnostics. Biosens Bioelectron. 2024;246:115875.
69. Raza A, Yusoff MZ. CNN-LSTM for motor imagery EEG. Eng Technol Appl Sci Res. 2025;15(3):22705–11.
70. Rejaibi E, Komaty A, Meriaudeau F, Agrebi S, Othmani A. MFCC-RNN for clinical depression detection. Biomed Signal Process Control. 2022;71:103107.
71. Rose DP. Wearable electronic sensors for sweat biomarkers. PhD thesis, Univ. of Cincinnati; 2016.
72. Rumbut J, Fang H, Carreiro S, Smelson D, Boyer E. Wearable biosensors for real-time substance use detection. IEEE IoT J. 2022;9(23):23405–15.
73. Saranya A, Subhashini R. Systematic review of XAI models. Decis Anal J. 2023;7:100230.
74. Sathyanarayanan S, Tantri BR. Confusion-matrix-based metrics. Afr J Biomed Res. 2024;27(4S):4023–31.
75. Savitzky A, Golay MJ. Smoothing and differentiation via least squares. Anal Chem. 1964;36(8):1627–39.
76. Shang L, Zhang Z, Tang F, Cao Q, Pan H, Lin Z. CNN-LSTM for ultrasonic guided waves. Sensors. 2023;23(16):7059.
77. Shbeeb RT, Mutlak FA. Gold/CeO_2 nanocomposites for photodetectors. Plasmonics. 2025;:1–16.
78. Siam AI, Sedik A, El-Shafai W, Elazm AA, El-Bahnasawy NA, El Banby GM, *et al*. Biosignal classification via CNNs. Int J Commun Syst. 2021;34(7):e4685.
79. Son SE, Cheon SH, Hur W, Lee HB, Kim DH, Ha CH, *et al*. One-step SlipChip for CRP detection. Biosens Bioelectron. 2024;243:115752.
80. Subburaj S, Liu C, Xu T. AI-integrated optical biosensors. Chem Commun. 2025.
81. Sun Q, Akman A, Schuller BW. Explainable AI for medical applications. ACM Trans Comput Healthc. 2025;6(2):1–31.
82. Sun Y, Zheng Y. Gas sensor drift compensation. Sci Rep. 2023;13(1):11971.
83. Duplicate of #82.
84. Tian H, Yu M, Liu X, Qian J, Qian W, Chen Z, *et al*. MoS_2/C anodes for lithium-ion batteries. Electrochim Acta. 2022;424:140685.
85. Upreti D, Yang E, Kim H, Seo C. Survey on federated learning in healthcare. CMES. 2024;140(3).
86. Uwaifo F, Uwaifo AO. Functionalized nanoparticle biosensor arrays patent. Nigeria Ministry of Industry; 2025.
87. van Geijn R. Tailoring Au size on Au/CeO_2 catalysts for RWGS reaction. 2025.
88. Varghese VM, Kavitha O, Poulose G, Joseph N. Trends in agricultural nanotechnology. Nanotechnol Appl Mod Agric. 2025;547–84.
89. Vimbi V, Shaffi N, Mahmud M. XAI (LIME/SHAP) in Alzheimer's detection. Brain Inform. 2024;11(1):10.
90. Wasilewski T, Kamysz W, Gębicki J. AI-assisted biosensing for early diagnosis. Biosensors. 2024;14(7):356.
91. Wong V, Fernandez L, Sankaran PKI, Holt A, Mishra R, Sinha V, *et al*. Workflow for partially reduced species in mAb manufacturing. Anal Biochem. 2023;666:115073.
92. Wu W, Huang Y, Wu X. Transformer-based heartbeat classification. Biomed Signal Process Control. 2024;88:105017.
93. Xu M, Li Y, Hu X, Zhang S, Liu Y. Smartphone-assisted colorimetric aptasensor for OTA detection. Microchem J. 2025;:115167.
94. Yang B, Zeng J, Zhao G, Ding C, Chen L, Huang Y. Gold-ceria cascade enzyme-mimicking sensor. Biosens Bioelectron. 2025;267:116847.
95. Duplicate of #94.
96. Zhao X, Li P, Xiao K, Meng X, Han L, Yu C. Sensor drift compensation with LSTM+SVM. Sensors. 2019;19(18):3844.
97. Zhao Y, Cao X, Lin J, Yu D, Cao X. Multimodal affective state recognition. IEEE Trans Affect Comput. 2021;14(2):1391–403.
98. Zhao Y, Sun T, Zhang H, Li W, Lian C, Jiang Y, *et al*. AI-enhanced electrochemical sensing for food safety. Biosensors. 2025;15(9):565.
99. Zhao Y, Wang Q, Li J, Ma H, Zhang Y, Wu D, *et al*. CeO_2-matrical ECL platform for PSA detection. 2016.
100. Zhou Y, Zhong S, Liu H, Zhu H, Zhu Z, Chen H. Peptide nanoparticle SERS tag for biosensing. Sens Actuators B Chem. 2024;412:135771.
101. Ziemba M. Mechanism of RWGS over Au/CeO_2 via operando spectroscopy. 2024.